Anomalous porosity preservation and preferential accumulation of gas hydrate in the Andaman accretionary wedge, NGHP-01 site 17A

Citation	Rose, K. K., Johnson, J. E., Torres, M. E., Hong, W. L., Giosan, L., Solomon, E. A., ... & Schaef, H. T. (2014). Anomalous porosity preservation and preferential accumulation of gas hydrate in the Andaman accretionary wedge, NGHP-01 site 17A. Marine and Petroleum Geology, 58, 99-116. doi:10.1016/j.marpetgeo.2014.04.009
DOI	10.1016/j.marpetgeo.2014.04.009
Publisher	Elsevier
Version	Version of Record
Terms of Use	http://cdss.library.oregonstate.edu/sa-termsofuse

Marine and Petroleum Geology 58 (2014) 99–116

Contents lists available at ScienceDirect

Marine and Petroleum Geology

journal homepage: www.elsevier.com/locate/marpetgeo

Research paper

Anomalous porosity preservation and preferential accumulation of gas hydrate in the Andaman accretionary wedge, NGHP-01 site 17A

Kelly K. Rose [a, b, *], Joel E. Johnson [c], Marta E. Torres [b], Wei-Li Hong [b], Liviu Giosan [d], Evan A. Solomon [e], Miriam Kastner [f], Thomas Cawthern [c, 1], Philip E. Long [g], H. Todd Schaef [h]

[a] National Energy Technology Laboratory, U.S. Department of Energy, Albany, OR 97321, USA
[b] College of Earth, Oceanic and Atmospheric Sciences, Oregon State University, Corvallis, OR 7331, USA
[c] Department of Earth Science, University of New Hampshire, Durham, NH 03824, USA
[d] Department of Geology and Geophysics, Woods Hole Oceanographic Institute, Woods Hole, MA 02543, USA
[e] School of Oceanography, University of Washington, Seattle, WA 98195, USA
[f] Scripps Institution of Oceanography, University of California, San Diego, La Jolla, CA 92093-0212, USA
[g] Lawrence Berkley National Laboratory, Berkeley, CA 94720, USA
[h] Pacific Northwest National Laboratory, Richland, WA 99352, USA

ARTICLE INFO

Article history:
Received 30 November 2013
Received in revised form
22 April 2014
Accepted 23 April 2014
Available online 6 June 2014

Keywords:
Porosity
Permeability
Grain size
Indian Ocean
Gas hydrate
Saturation
Volcanic ash
Carbonate

ABSTRACT

In addition to well established properties that control the presence or absence of the hydrate stability zone, such as pressure, temperature, and salinity, additional parameters appear to influence the concentration of gas hydrate in host sediments. The stratigraphic record at Site 17A in the Andaman Sea, eastern Indian Ocean, illustrates the need to better understand the role pore-scale phenomena play in the distribution and presence of marine gas hydrates in a variety of subsurface settings. In this paper we integrate field-generated datasets with newly acquired sedimentology, physical property, imaging and geochemical data with mineral saturation and ion activity products of key mineral phases such as amorphous silica and calcite, to document the presence and nature of secondary precipitates that contributed to anomalous porosity preservation at Site 17A in the Andaman Sea. This study demonstrates the importance of grain-scale subsurface heterogeneities in controlling the occurrence and distribution of concentrated gas hydrate accumulations in marine sediments, and document the importance that increased permeability and enhanced porosity play in supporting gas concentrations sufficient to support gas hydrate formation. The grain scale relationships between porosity, permeability, and gas hydrate saturation documented at Site 17A likely offer insights into what may control the occurrence and distribution of gas hydrate in other sedimentary settings.

Published by Elsevier Ltd.

1. Introduction

Natural gas hydrates, ice-like crystalline compounds composed of water molecules surrounding molecules of natural gas, occur in a variety of geologic environments. Most commonly, natural gas hydrates (NGHs) are found in marine sediments where conditions supporting the formation of the gas hydrate stability zone (GHSZ) exist, including high pressures and low temperatures (Sloan and Koh, 2008) and abundant methane to establish the clathrate structure. Globally, estimates of NGH occurrences vary, (Frye, 2008; Frye et al., 2013; Johnson, 2011; Kvenvolden, 1988; Kvenvolden and Lorenson, 2000; MacDonald, 1990; Max et al., 2006; Milkov, 2004), however most estimates agree that significant abundances of organic carbon are trapped in NGH accumulations predominantly as methane gas (250,000 to 1,250,000 trillion cubic feet). In the marine environment, sediments in the GHSZ are often associated with slope and basin settings. These settings are dominantly composed of fine-grained silt and clay lithofacies with generally low vertical permeability, and pore fluids are frequently under-

* Corresponding author. National Energy Technology Laboratory, U.S. Department of Energy, Office of Research and Development, 1450 Queen Avenue SW, Albany, OR 97321, USA. Tel.: +1 541 967 5883.
E-mail addresses: Kelly.rose@netl.doe.gov, rosek@science.oregonstate.edu (K.K. Rose).
[1] Now at Department of Geography and Geosciences, Salisbury University, Salisbury, MD 21801, USA.

http://dx.doi.org/10.1016/j.marpetgeo.2014.04.009
0264-8172/Published by Elsevier Ltd.

saturated with respect to methane, the most common natural gas found in hydrate systems on Earth (Sloan and Koh, 2008). As a result, while the conditions for the GHSZ may be widely present in appropriate marine settings, the distribution of NGH in the subsurface is neither ubiquitous nor uniform.

Field and laboratory studies have shown that the controls on the distribution and occurrence of NGH in marine sediments vary and are largely tied to site-specific factors including but not limited to, sediment composition and grain size, the nature and volume of the gas source, pathways and mode of gas migration, pore-fluid chemistry, and the porosity and permeability of the host strata. Studies from regions such as the Cascadia Margin (Malinverno, 2010; Malinverno et al., 2008; Torres et al., 2008; Trehu et al., 2004), the Gulf of Mexico (Boswell et al., 2012; Collett et al., 2012; Cook and Malinverno, 2013; Lee et al., 2012), and Nankai trough (Uchida et al., 2009) have demonstrated that NGH will preferentially form at higher concentrations in more porous and permeable sedimentary layers, such as sand and volcanic ash beds. There is growing evidence that properties such as grain size, composition, and gas migration may contribute to complex distributions of gas hydrate saturation within porous-permeable reservoirs themselves (Boswell et al., 2011, 2012; Collett et al., 2011, 2012; Lee and Collett, 2011; Lee et al., 2012; Rose et al., 2011). Field, modeling, and laboratory studies (Kneafsey et al., 2009; Lu et al., 2011; Malinverno, 2010; Shankar and Riedel, 2013; Torres et al., 2008) indicated that for the majority of marine systems, which are dominantly fine-grained with discrete, well-constrained porous and permeable layers, a general relationship exists between higher NGH saturations and grain size of the host sediment. However, studies of NGH accumulations both onshore (Collett et al., 2012; Rose et al., 2011) and offshore (Bahk et al., 2011, 2014, 2013; Collett et al., 2012; Torres et al., 2008) increasingly illustrate that hydrate distribution within the GHSZ does not always have a simple relationship with grain size.

The research presented here takes advantage of sediment core and borehole related data recovered by drilling at Site 17 in the Andaman Sea during the Indian National Gas Hydrate Program Expedition 1 (NGHP-01) in 2006, to investigate reservoir-scale controls on gas hydrate distribution. From the cored borehole, Site 17A, we recovered low concentrations of NGH throughout most of the GHSZ, however, higher NGH saturations were consistently observed within the more porous and permeable volcanic ash-bearing intervals (Collett et al., 2008). To enhance our understanding of the mechanisms that lead to the observed NGH distribution, we conducted additional analyses lithology (including composition and grain size), and dissolved silica and calcium. We used a scanning electron microscope (SEM) with a back-scatter electron detector (BSE) and energy dispersive spectroscopy (EDS) to conduct image and compositional analyses of select sediment samples at Site 17A. These data were integrated with field lithostratigraphic and post-cruise datasets in order to evaluate the role that sediment composition, texture, and the occurrence and distribution of secondary precipitates play in enhancing gas hydrate saturation at Site 17A.

We show that the porosity profile observed in borehole geophysical data and physical properties measured in core samples (Collett et al., 2008) at Site 17A relative to the expected profile (see Hamilton, 1976) for a calcareous nannofossil ooze is anomalous. In particular, at Site 17A the porosity profile is enhanced relative to expected porosity from 225 m below seafloor (mbsf) to total depth (TD) of the well as a result of secondary mineral precipitates. When this relationship is evaluated against grain size measurements for the entire sediment core interval, and gas hydrate saturations (Collett et al., 2008), we show that hydrate occurrence greater than 10% of the pore volume preferentially occurs in coarser grained, and more well sorted lithofacies. This relationship illustrates the complex balance and lithology-driven controls on hydrate accumulations of higher concentrations.

2. Geologic setting

2.1. Tectonic and sedimentary setting

The Andaman-Sunda basin formed as a result of subduction of the Indian Plate beneath the Sunda Plate over the past ~65 Ma (Pal et al., 2003) (Fig. 1). The Andaman Island Arc complex lies in the central portion of the 5000 km long Burma-Sunda-Java subduction complex (Pal et al., 2003). NGHP-01 Site 17A (Fig. 1) is located within the accretionary wedge along the Andaman-Sunda portion of this complex near the plate boundary between the Indian Plate and the Sunda Plate (Curray, 1979; Curray, 2005; Curray and Moore, 1974). East of the Andaman-Sunda arc complex, backarc extension, initiated between 11 and 4 Ma resulted in the present day Andaman basin (Pal et al., 2003; Raju et al., 2007; Rodolfo, 1969). The Andaman-Sunda wedge, forearc, and back-arc, is dominated by regional reverse, extensional, and transform faults that strike roughly parallel with the north–south axis of the Andaman Trench (Krishna and Sanu, 2002; Rodolfo, 1969). In addition, tectonic folds of varying amplitude are also pervasive throughout the western portion of the region. These compressional folds are part of the accretionary wedge, which lies between the extensional Eastern Margin Fault and compressional Diligent Fault (Cochran, 2010). NGHP-01 Site 17A (Fig. 1) sits near the crest of a broad anticlinal fold which is underlain by the Diligent Fault in the Andaman accretionary wedge to the east of Little Andaman Island (Cochran, 2010; Collett et al., 2008).

Deposition in the northern portion of the Andaman basin is dominated by siliciclastic sedimentation. These include Miocene to recent age deposits, primarily sourced from the Irrawaddy Delta system (Mohan et al., 2006). Irrawaddy siliciclastics are delivered from the northern shelf into the Andaman basin primarily via turbidity flows. However, bathymetric complexities, including the Andaman-Nicobar Ridge that lies between the deltaic source and the Nicobar Deep, may restrict the transport of Irrawaddy derived sediments to the northern Andaman basin. The lithologic sequence at NGHP-01 Site 17A, situated in the Andaman wedge, is dominated by pelagic (biogenic dominated) sedimentation (Collett et al., 2008; Cawthern et al., 2014), receiving little to no coarse siliciclastics from the adjacent land masses (Fig. 1). Structural down warping on the outboard side of the Andaman margin results in a low geothermal gradient and marine biogenic organic matter present throughout the section supports methane production (Johnson et al., 2014). Both of these conditions support the occurrence of an anomalously thick GHSZ in this basin, which at NGHP-01 Site 17A extends from the seafloor to 605 mbsf (Collett et al., 2008).

Drilling and coring at Site 17 confirmed the presence of methane hydrate-bearing sediments and provided information about the conditions that produced these accumulations (Collett et al., 2008). The dominant lithologies observed in cores recovered from NGHP-01 Site 17A were biogenic oozes. The sedimentary record throughout the Andaman Basin is also punctuated by distinct, volcanic ash beds recording the volcanic history of the arc from the Cenozoic to the present (Cawthern et al., 2010; Rodolfo, 1969). The ash layers at Site 17A that serve as the dominant host lithology for NGH occurrences are related to volcanic activity in the Andaman region since the Miocene (Cawthern et al., 2010; Collett et al., 2008).

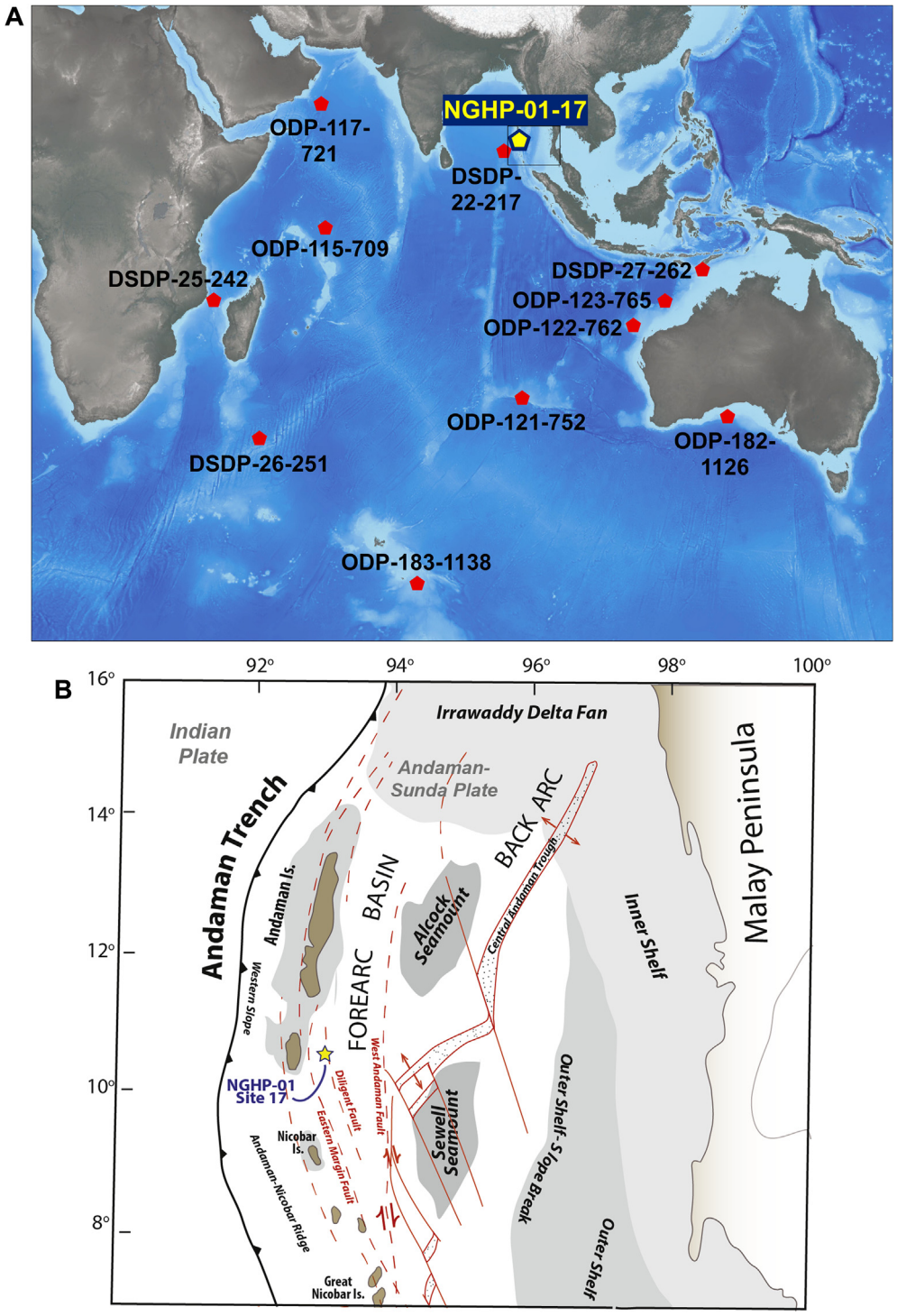

Figure 1. A. Location map showing the location of NGHP-01-17A and selected ODP and DSDP core locations where data is used in this study. B. Key tectonic and geographic features map in the Andaman Sea (based on maps from Cochran (2010) and Rodolfo (1969).

2.2. Hydrocarbon setting

The Andaman Basin does not have a significant history of conventional oil or natural gas production. Limited conventional hydrocarbon exploration has been conducted in this region. As part of the New Exploration Licensing Policy (NELP) of India's Directorate General of Hydrocarbons, Mohan et al. (2006) evaluated the potential for conventional hydrocarbon resources in the Andaman Basin and documented the occurrence of natural gas in one well that targeted mid-Miocene limestones to the east of Site 17A. This study along with a few other wells drilled in the Andaman Basin (Bastia and Radhakrishna, 2012; Chakraborty et al., 2013) corroborates the presence of a deep natural gas source in the region.

Pre-drill 3D seismic interpretations (Cochran, 2010; Collett et al., 2008) revealed an unusually deep (~605 mbsf), but regionally pervasive bottom simulating reflector (BSR). With the exception of

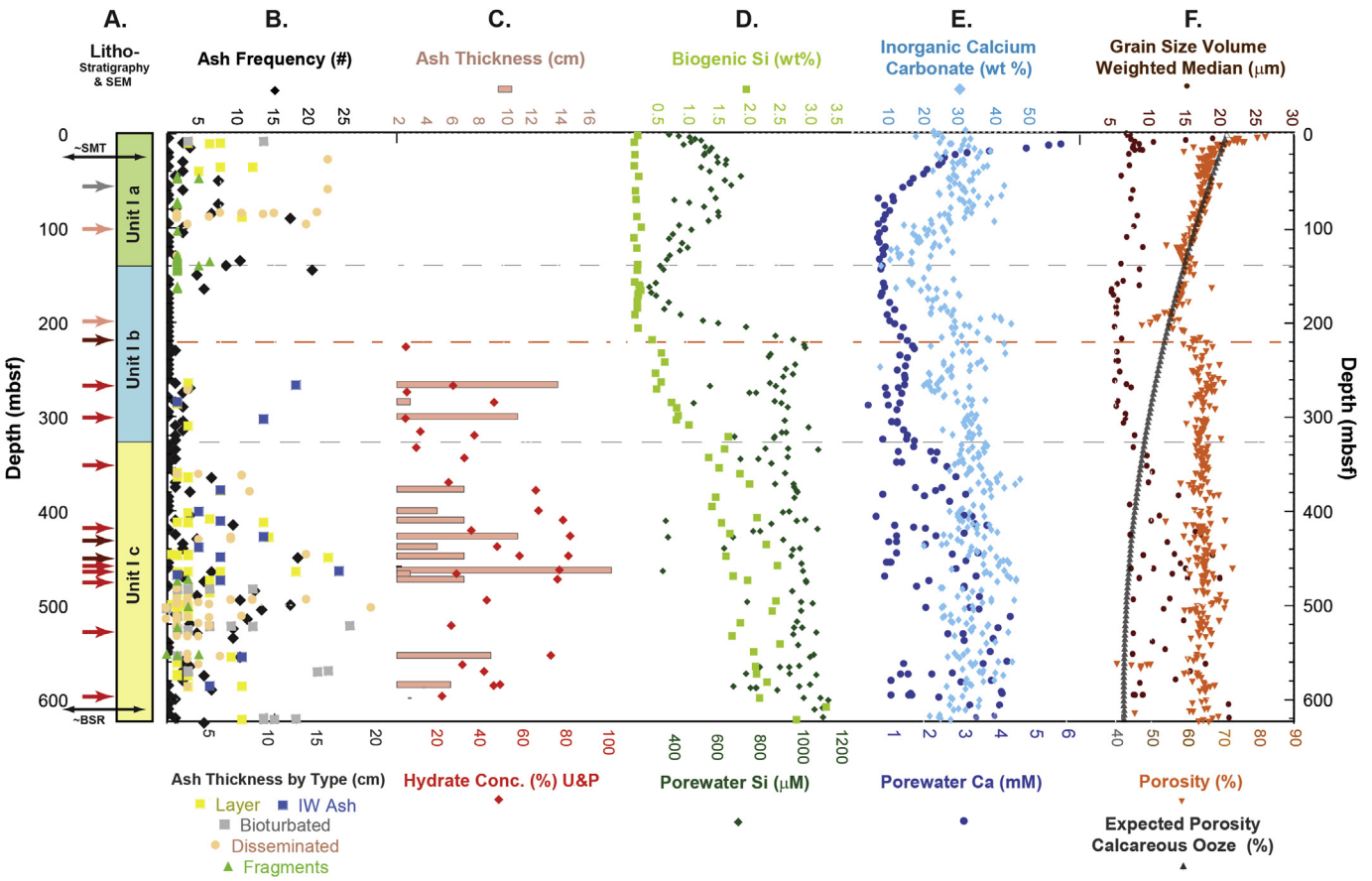

Figure 2. Plots comparing key lithostratigraphic, physical property, and geochemical data from NGHP-01 Site 17A. A) Lithostratigraphy summary of Site 17A showing the location of the 3 primary lithostratigraphic subunits at this site and the locations of SEM samples, arrows. The color of the arrows corresponds to relative abundance of authigenic carbonate observed in each SEM sample, gray = none, pink = rare, red = common, dark red = abundant, B) Ash frequency plot (histogram based on number of ash occurrences of a given thickness versus depth, see Collett et al., 2008 for data), ash thickness, and ash occurrence type versus depth, C) Comparison of volcanic ash layer thicknesses associated with porewater geochemistry samples versus estimated hydrate saturations based on (Ussler and Paull, 2001), D) Comparison of porewater silica concentrations (μM) and biogenic silica volumes (wt %) versus depth, E) Comparison of total calcium carbonate volumes (weight %) and porewater calcium (mM) concentrations versus depth, and F) Expected calcareous ooze porosity curve (Hamilton, 1976), actual Site 17A porosity profile, and median grain size profile versus depth. (SMT = Sulfate–Methane Transition; BSR = Bottom Simulating Reflector based on data from Collett et al., 2008). Gray dashed lines align with lithostratigraphic subunit boundaries, and the red dashed line aligns with the depth of anomalous porosity preservation. (For interpretation of the references to color in this figure legend, the reader is referred to the web version of this article.)

the deep, through-going BSR, and limited conventional hydrocarbon indicators (Mohan et al., 2006), evidence for an NGH system in the Andaman basin prior to the NGHP-01 expedition was limited.

2.3. NGHP-01 site 17A lithostratigraphy

NGHP-01 Site 17A is located in the Andaman Sea to the east of the Andaman-Nicobar Islands (10° 45.1912′N, 93° 6.7365′E), at a water depth of ~1344 m (Collett et al., 2008) (Fig. 1). Site 17 includes one well, NGHP-01-17A, drilled and cored by D/V JOIDES Resolution to depths of 692 mbsf. As a result of poor borehole conditions in NGHP-01-17A, a second, offset well, NGHP-01-17B, was drilled exclusively for borehole geophysical logs and surveys. Well 17B, in ~1350 m of water and located 20 m south of well 17A, was drilled to a total depth of 718 mbsf, to ensure a deep enough borehole to acquire borehole geophysical data across the BSR (Collett et al., 2008). The lithostratigraphic framework for Site 17A was developed based on wireline logging data, physical property measurements, and split core descriptions, including 184 subsamples used for sedimentologic analysis of major and minor lithofacies (Collett et al., 2008).

The sedimentary sequence at Site 17A consists of one lithostratigraphic unit divided into three Subunits, Ia, Ib, and Ic, composed of nannofossil oozes for its entire 692 m (Collett et al., 2008). Based on calcareous nannofossil biostratigraphy (Abel-Flores et al., 2014), this sequence represents a record spanning the past 9.4 Ma. Shipboard sedimentologic analyses and physical property measurements were used to differentiate the three nannofossil Subunits at Site 17A (Collett et al., 2008). Subunit Ia, from 0 to 137 mbsf, distinguished by significant amounts of carbonate biogenic forms, is a foraminifera -rich to -bearing nannofossil ooze (Fig. 2A). Subunit Ib, from 137 to 335 mbsf, is mainly a nannofossil ooze, however, from ~155 to ~195 mbsf this subunit notably includes authigenic carbonate -bearing to -rich nannofossil ooze (Fig. 2A). Subunit Ic, from 336 to 692 mbsf, is characterized by an increase of siliceous biogenic materials and is a diatom -bearing to -rich, and sponge spicule -bearing to -rich nannofossil ooze (Fig. 2A). In this study we seek to understand the relationship between the Site 17A sedimentary framework and areas of high gas hydrate saturation, through comparison of shipboard porewater geochemistry, physical property and lithostratigraphic datasets with newly acquired grain size analyses of major and minor lithofacies; petrographic evaluation via SEM and BSE of sediment composition and texture; estimates of silica and carbonate saturation; and evaluation of the quantified biogenic silica and bulk $CaCO_3$ fraction.

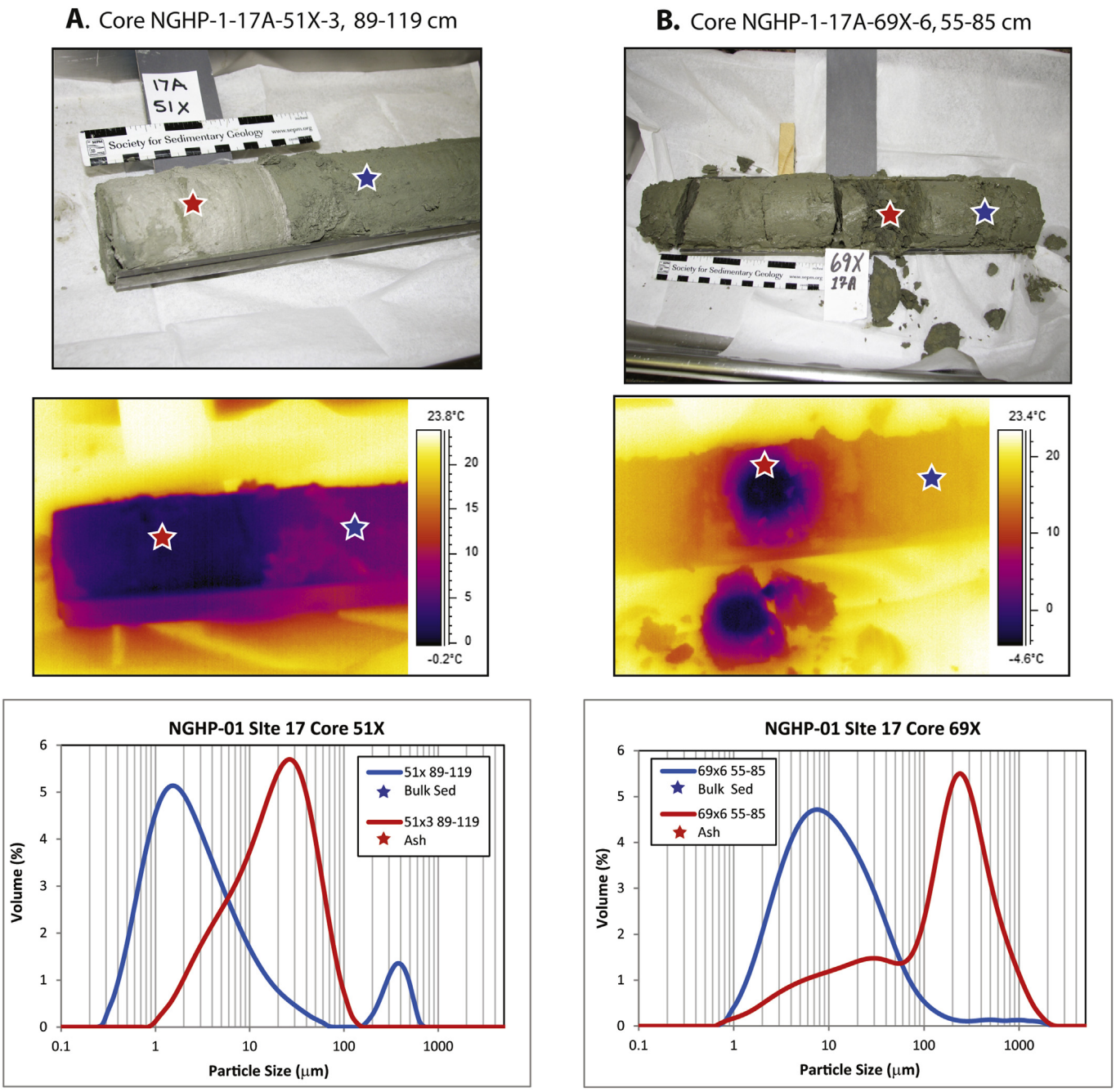

Figure 3. Corresponding core photographs, IR images, and grain size distribution profiles from two porewater sediment samples (A and B) representative of the correlation between IR thermal anomalies and the occurrence of volcanic ash layers (red stars and curves) versus bulk sediment (blue stars and curves) that is observed at NGHP-01 Site 17A between 220 mbsf and the BSR at 605 mbsf. (For interpretation of the references to color in this figure legend, the reader is referred to the web version of this article.)

3. Methods

3.1. Particle size analysis

Grain size distribution of samples from discrete volcanic ash samples as well as bulk sediment samples spanning from 0 to 683 mbsf of the sediment profile at NGHP-01 Site 17A were measured using a Malvern Mastersizer 2000 laser-diffractometer particle size analyzer with Hydro-G dispersion unit. Approximately 0.5 cm^3 of sediment was suspended in a solution of 20 mL of 5.4 g/L sodium hexametaphosphate, agitated, left for >12 h prior to analysis (Sperazza et al., 2004). Each sample was dispensed into the Hydro-G dispersion unit which kept the sample suspended in the water tank via mechanical stirring. If necessary, water was added to dilute the water-sample mixture until the ideal obscuration rate of 15 and 20% was obtained. The sample was then subjected to 60 s of sonication in the tank to prevent flocculation before being processed by the Mastersizer 2000 laser-diffractometer for analysis.

A total of 70 bulk sediment samples taken from original NGHP-01 Site 17A sedimentology CHN plugs were used to measure and profile the background grain size distribution of all lithogenic, biogenic, and authigenic components throughout the core from Site 17A. During shipboard operations porewater geochemistry samples

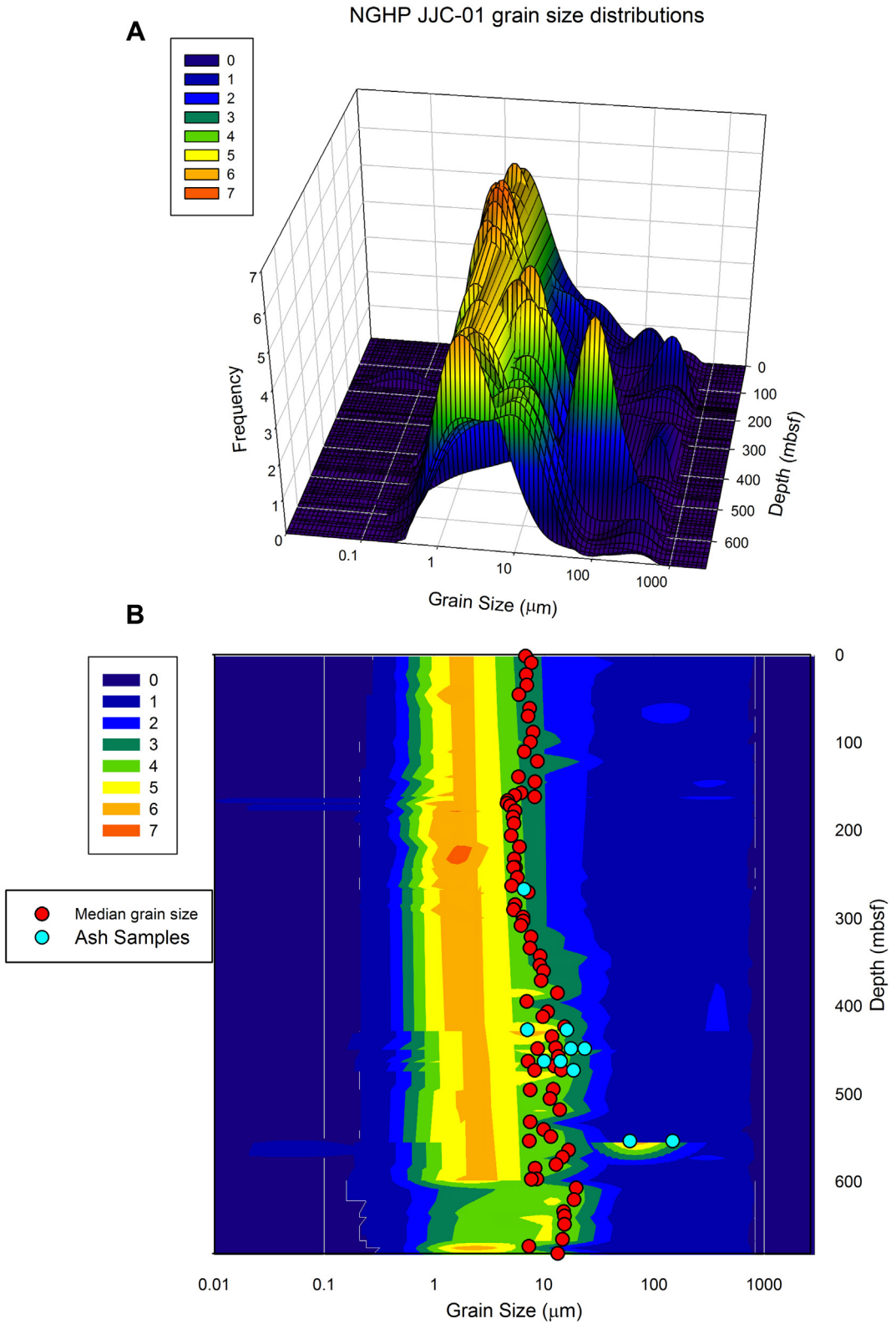

Figure 4. A. Grain size distributions of bulk sediment and volcanic ash samples. Horizontal axis is grain size from 0 to 1000 μm, left vertical axis is percentage of the total distribution (frequency), and right horizontal axis is depth in mbsf. B. This plot portrays the same grain size distribution frequency data interpolated with depth and also displays median grain size for bulk sediment (red dots) and volcanic ash samples (blue dots) versus depth (mbsf). (For interpretation of the references to color in this figure legend, the reader is referred to the web version of this article.)

containing volcanic ash-rich layers were sometimes separated into two derivative subsamples, where the ash-rich section of the core was separated from the surrounding bulk sediment (Fig. 3). These porewater subsamples were squeezed and preserved separately. As a result, a subset of 17A samples from porewater geochemistry squeeze cakes were also used to obtain grain size distribution profiles for 10 volcanic ash layers for which 5 subsamples of associated background sediment samples were also used (Figs. 4 and 5).

3.2. Petrographic analyses

Seventeen Site 17A sediment samples were evaluated using an FEI Inspect F, Field Emission SEM and Oxford Instruments INCA X-ray analyzer on polished epoxy-impregnated mounts. The SEM examination included BSE imaging and microanalysis energy dispersive spectroscopy (EDS). Samples analyzed by SEM came from 10 bulk sediment samples and 7 volcanic ash layers (Table 1) from Site 17A, spanning depths between 53 and 599 mbsf. Several samples were selected from the porewater geochemistry set that coincided with hydrate-bearing, volcanic ash-rich layers. The remaining porewater and bulk sediment samples were selected to be representative of the background host sediment, thus providing a visual and compositional analysis of major and minor lithologies present at NGHP-01 Site 17A.

All sediment samples were mounted in epoxy, polished, and vacuum coated with palladium prior to analysis. Each sample was examined using the SEM and a visual estimate of the sample composition, including secondary precipitates and features, was made for each sample. Relative abundance of key sediment components of each sample were made based on the visual estimation method of Terry and Chilingar (1955) where trace abundances were categorized as present but at 3% or less of the total sample, rare occurrences were 3–5%, common occurrences were 5–20%, and abundant occurrences were observed at >20% of the total sample. Select quantitative measurements using elemental X-ray mapping were utilized to confirm visual evaluations and assess the composition of major lithogenic, biogenic, and diagenetic particles present in each sample by their intensities in EDS X-ray maps and/or spot analyses. Elemental concentrations for quantification were optimized using a Cu-Kα standard (Goldstein et al., 1997).

3.3. Biogenic silica

Approximately 25 mg of dried sediment was subjected to leaching of BSi using a wet alkaline method (e.g. DeMaster, 1981; Mortlock and Froelich, 1989), followed by measurement of leached silica on a Spectronic 601 UV–Vis spectrophotometer (Strickland and Parsons, 1972). Leaching over five hours with subsamples collected at each hour, allowed for the precise determination of biogenic silica by accounting for leaching of silicate minerals, as described in Cawthern et al. (2014) (Fig. 2D). Samples for biogenic silica analyses were selected from ash-free sediment layers.

3.4. Inorganic calcium carbonate

Weight percent (wt. %) $CaCO_3$ was determined by difference from measured total carbon (TC) and total organic carbon (TOC) from 417 bulk sediment samples spanning the Site 17A record (Fig. 2E) using a Perkin Elmer 2400 Series II CHNS Elemental Analyzer as described in Johnson et al., (this volume). Given the high $CaCO_3$ content at NGHP-01-17A an improved sample mass and acidification approach was developed (Phillips et al., 2011) to obtain the most accurate TC and TOC measurements (and thus derivative IC) at Site 17A and several other NGHP-01 sites. Separate 10 mg splits from the same bulk sediment sample were used for the TC and TOC measurements. Reproducibility was established by running replicate samples and calculating the standard deviation. Duplicate samples were run approximately every 10 samples by depth. Soil standards were run every 10 samples for quality control and blanks and acetanilide ($C_6H_5NHCOCH_3$) standards were run every 20 samples to ensure proper instrument operation After all samples were analyzed, outliers where re-measured. $CaCO_3$ wt. % was calculated by multiplying the derivative IC wt. % by 8.331779 to account for the non-carbon mass fraction. Errors (2σ) of TC and TOC were summed in quadrature to obtain IC and $CaCO_3$ error. Average reproducibility for TC, TOC, and $CaCO_3$ were 0.10, 0.04, and 0.83 wt. % respectively.

3.5. Porewater data

Porewater sampling and shipboard analyses procedures are detailed in Collett et al. (2008). Further analytical details are given in Solomon et al. (2014). Alkalinity and pH were measured immediately after squeezing via a titanium squeezer modified after the stainless-steel squeezer of Manheim and Sayles (1974), following the procedures in Gieskes et al. (1991). The pH was measured with a combination glass electrode, and alkalinity was determined by Gran titration with an autotitrator. Three to five mL of IW was titrated with 0.1 N HCl at 25 °C. Chloride concentrations were measured by titration with $AgNO_3$, with the percent precision of chloride values averaging 0.2%. Subsamples were collected for post cruise analyses of major ions and dissolved silica.

Concentrations of major cations (Na, Mg, K, Ca) are measured by external calibration on a Leeman Labs Prodigy ICP-OES at Oregon State University. Calibration standards are diluted from primary solutions in 1% sub-boiling-distilled HNO_3, and samples are diluted 100-fold by volume in 1% HNO_3 prior to measurement. Accuracy, determined by repeat analysis of IAPSO Standard Seawater, with a practical salinity of 34.993 is better than 1.2% RSD (1-sigma).

Pore fluid samples were analyzed for dissolved silica concentrations on a ThermoScientific Genesys 10s Vis spectrophotometer using the colorimetric method described in Gieskes et al. (1991), which is based on the production of a yellow silicomolybdate complex and the subsequent reduction of this complex to yield a blue color. Absorbance was read on the spectrophotometer at a wavelength of 812 nm. Calibration, check, and drift standards were made from a 3000 μM stock solution prepared by dissolving 0.5642 Na_2SiF_6 in 1000 ml of ultrapure water. The average precision of the dissolved silica analyses based on repeated measurement of the 480, 300, and 500 μM matrix-matched standards over a 1-month period was <1%, and the average accuracy based on repeated analysis of the 300 and 500 μM check standards was <1.5%.

3.6. Geochemical modeling, saturations and activities

The mineral saturation and the ion activity products were calculated by using CrunchFlow (Steefel, 2009), a FORTRAN-based software to model multicomponent reactive flow and transport. The software fits a polynomial to the thermodynamic data from the 9 temperature points from 0 to 25 °C so that the solubility can be obtained from any temperature within this range. Saturations under different pressures were calculated using SUPCRT92, a software package for calculating standard molal thermodynamic properties (Johnson et al., 1992). Ion activity coefficients are calculated with an extended Debye–Hückel formulation (Steefel, 2009), which considers the radius of a point charge, the ionic strength of the solution, and the charge of the ion. The temperature dependence of this coefficient is from EQ3/EQ6.

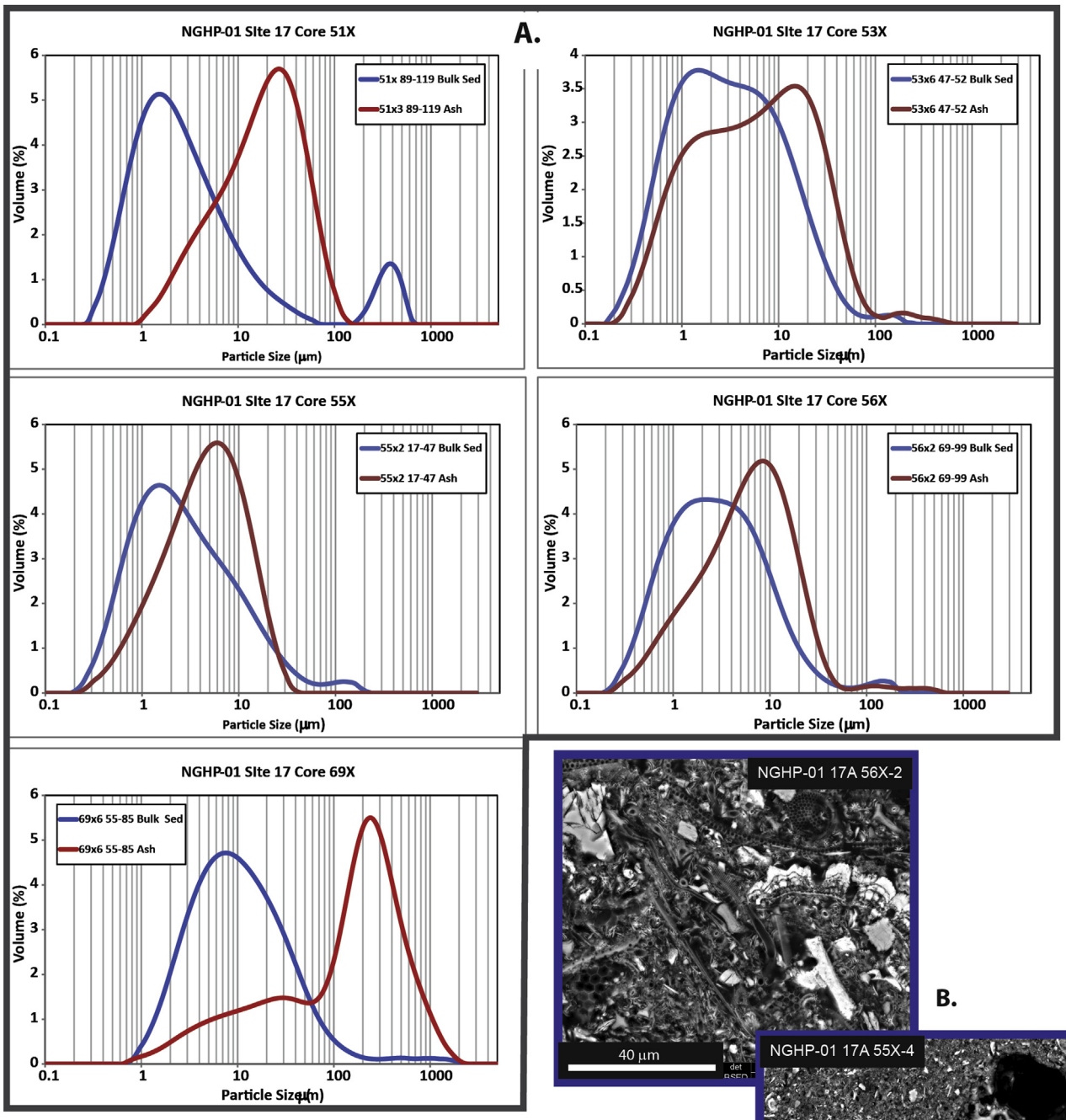
A.
NGHP-01 SIte 17 Core 51X
51x 89-119 Bulk Sed
51x3 89-119 Ash
Volume (%)
Particle Size (μm)
NGHP-01 SIte 17 Core 53X
53x6 47-52 Bulk Sed
53x6 47-52 Ash
Volume (%)
Particle Size (μm)
NGHP-01 SIte 17 Core 55X
55x2 17-47 Bulk Sed
55x2 17-47 Ash
Volume (%)
Particle Size (μm)
NGHP-01 SIte 17 Core 56X
56x2 69-99 Bulk Sed
56x2 69-99 Ash
Volume (%)
Particle Size (μm)
NGHP-01 SIte 17 Core 69X
69x6 55-85 Bulk Sed
69x6 55-85 Ash
Volume (%)
Particle Size (μm)

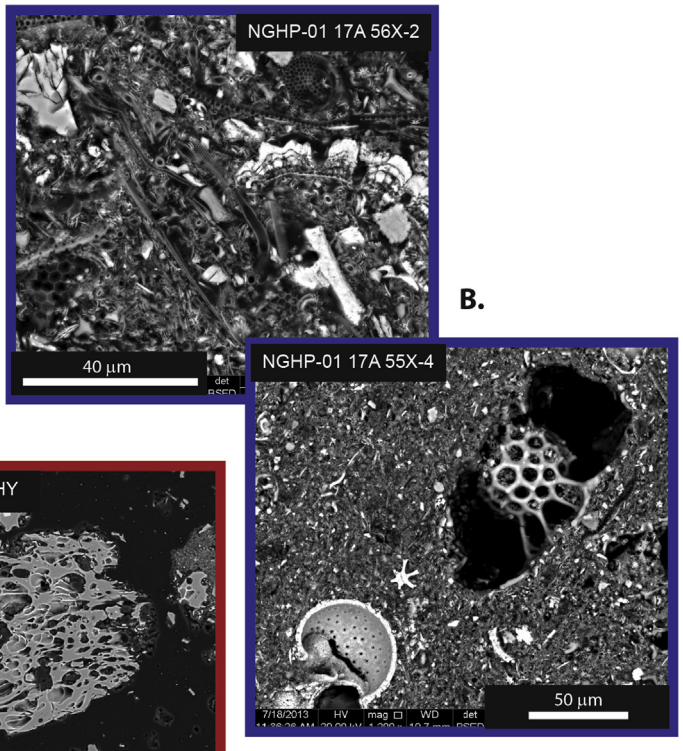
NGHP-01 17A 56X-2
40 μm
B.
NGHP-01 17A 55X-4
50 μm

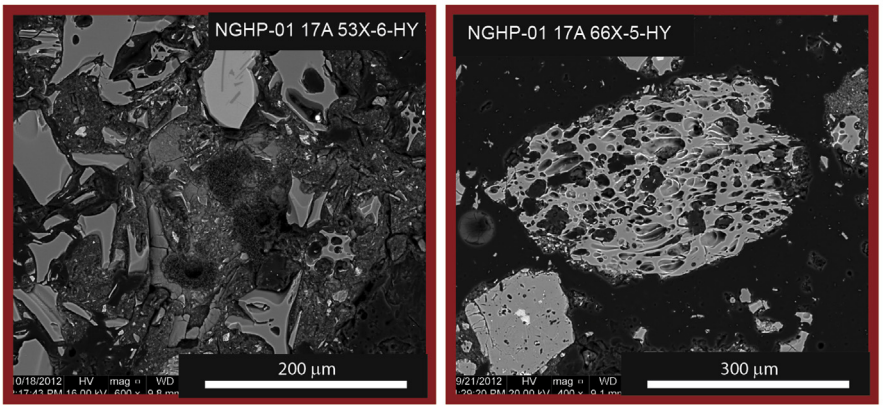
NGHP-01 17A 53X-6-HY
200 μm
NGHP-01 17A 66X-5-HY
300 μm
C.

Table 1
Summary of SEM samples analyzed from NGHP-01 Site 17A with visual estimates of secondary carbonate and secondary silica abundances. For porewater related samples, volcanic ash thicknesses and hydrate concentrations are also provided.

SEM Sed sample type	SEM sample ID	Depth (mbsf)	Ash thickness (cm)	Hydrate conc (%) U&P	2nd Carbonate	2nd Silica	Lithstrat Unit
Bulk Sed	7H-2	54					Ia
Bulk Sed	12H-1	100			Trace		Ia
Bulk Sed	23X-4	199			Trace		Ib
Bulk Sed	25X-1	214	No analysis, poor sample				Ib
Bulk Sed	27X-1	233			Abundant		Ib
Porewater	30X-6-HY	268	12	27	Common	Trace	Ib
Porewater	34X-4-HY	303	9	4	Common		Ib
Bulk Sed	41X-2	349			Common		Ic
Porewater	50X-4	419			Common		Ic
Porewater	51X-3-HY	428	9.5	81	Abundant	Rare	Ic
Porewater	53X-6-HY	450	5	80	Abundant	Trace	Ic
Porewater	55X-2-HY	464	16	76	Common	Trace	Ic
Bulk Sed	55X-4	465			Common	Trace	Ic
Bulk Sed	56X-2	474			Common	Trace	Ic
Porewater	56X-2-HY	474	5	75	Common	Rare	Ic
Porewater	66X-5-HY	555	7	71	Common	Rare	Ic
Bulk Sed	73X-2	599			Common		Ic

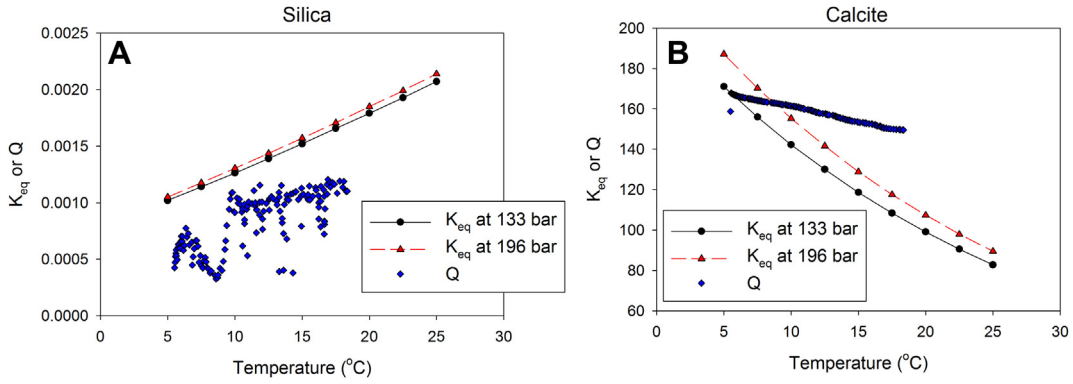

Figure 6. Temperature-dependent thermodynamic data corresponding to two different pressures (133 and 196 bar which equate to 1344 m water depth at the sea floor at NGHP-01 Site 17A, and 2000 m water depth respectively) were computed and plotted as the solid lines for amorphous silica (A) and calcite (B). Ion activity products, based on analysis of activities of pore water Si, Ca, HCO_3^-, and H^+, were calculated with respect to amorphous silica (A) and calcite (B) were then calculated and plotted against temperature. Ion activity products falling above the K_{eq} lines fall in the realm of mineral precipitation. Products plotting below K_{eq} lines reside in the realm of mineral dissolution.

Two minerals were targeted in this study, calcite ($CaCO_3$) and silica (SiO_2). Two sets of temperature-dependent thermodynamic data that correspond to two different pressures (133 and 196 bar which equate to 1344 m water depth at the sea floor at NGHP-01 Site 17A, and 2000 m water depth respectively) were computed and plotted as the solid lines on Figure 6. The activities of pore water Si, Ca, Mg, HCO_3^-, and H^+ were generated by CrunchFlow after assigning pore water composition, temperature, and pH. Temperature of each sampling depth was estimated from the geothermal gradient (2.1 °C/100 m) and bottom seawater temperature (5.5 °C) measured at Site 17A (Collett et al., 2008). Ion activity products with respect to the three target minerals were then calculated and plotted against temperature as shown in Figure 6.

3.7. Infrared imaging

Infrared imaging (IR) enabled the detection of thermal anomalies indicative of the presence of gas hydrates in cores prior to their removal from the core liner. IR imaging thus served as a crucial guide to sampling for pore water chemistry per the protocol established by Long et al. (2010).

4. Results

4.1. Grain size analyses and trends

Grain size measurements at NGHP-01 Site 17A were conducted on 77 bulk sediment samples (Fig. 3). In addition, grain size measurements were conducted on 10 volcanic ash layer samples (Fig. 3B) that were associated with significant gas hydrate accumulations and were originally sampled for pore water analyses (Figs. 4A, B, and 5). The bulk sediment grain size distribution reveals a predominantly very fine to fine silt size fraction (Folk, 1966; Wentworth, 1922). The volume weighted median grain size ($d(0.5)$) ranges from 4 to 15 μm, but the overall distribution spans from clay to sand grain size fractions (Fig. 3). The 10th percentile of the grain size distribution ($d(0.1)$) for Subunit Ia ranges from 1.9 to 2.3 μm, for Subunit Ib from 1.3 to 2.4 μm, and for Subunit Ic from 2.1 to 3.3 μm.

Figure 5. A) Grain size distribution curves for five samples where there was hydrate-bearing ash and associated bounding, bulk sediment. In all samples the ash curves are skewed to varying degrees toward the 1–5 um interval which corresponds to the same grain size range of secondary carbonate grains found in all of these samples. B) SEM images of bulk sediment samples from NGHP-01 Site 17A, C) SEM images of volcanic ash-rich samples from NGHP-01 Site 17A.

The median grain size ($d(0.5)$) for Subunit Ia ranges from 6.2 to 7.3 μm, for Subunit Ib from 4.8 to 6.2 μm, and for Subunit Ic from 7.4 to 13.2 μm. The 90th percentile ($d(0.9)$) grain size distribution for Subunit Ia ranges from 43.9 to 70.4 μm, for Subunit Ib from 29.8 to 80.8 μm, and for Subunit Ic from 31.9 to 84.2 μm. Thus the 10th, 50th, and 90th grain size fractions for the bulk sediment samples at Site 17A demonstrate the overall, slightly coarser grained nature of Subunit Ic (Fig. 3) relative to Subunits Ia and Ib.

The ten volcanic ash-rich samples selected for analysis show a much broader range of volume weighted median grain sizes ($d(0.5)$), ranging from very fine silt size at 6 μm to fine sand size at 159 μm (Fig. 3B) (Folk, 1966; Wentworth, 1922). However, the grain size distributions for most of the volcanic ash samples showed a much tighter range, less variability, per sample than most of the bulk sediment samples (Figs. 3–5). The $d(0.1)$ grain size distribution for the twelve ash samples ranges from 1.9 to 7.1 μm, with an average $d(0.1)$ of 3.5 μm. The $d(0.5)$ for the ash samples ranges from 5.9 to 159 μm, with an average $d(0.5)$ of 32 μm, and the $d(0.9)$ for the ash samples ranges from 36.5 to 533 μm with an average $d(0.9)$ of 129 μm. For individual ash samples, the grain size distributions generally show a tighter or bimodal profile than the bulk sediment samples, indicating better sorting than that of the bulk sediment (e.g. Figs. 4 and 5).

Generally, the bulk sediment volume weighted median grain size showed a good correlation with the downcore lithostratigraphic subunit depths at Site 17A (Fig. 2A and F). The average median grain size for samples measured in Subunit Ia is 7.6 μm, Subunit Ib is 6.3 μm, and Subunit Ic is 14.9 μm (Fig. 3). The slightly coarser median grain size of Subunits Ia and Ic are influenced by the presence of foraminifera and volcanic ash fragments in Subunit Ia and diatoms and volcanic ash frequency in Subunit Ic (Fig. 2A, B and F). In Subunit Ic, the median grain size gradually increases from the top of this Subunit to a depth of ~400 mbsf where the median grain size and grain size distributions increase notably from 400 mbsf to 605 mbsf and are slightly coarser than the shallower sedimentary sequence at Site 17A (Figs. 2A, B, F, and 3). This increase in grain size and grain size distribution from ~400 to 605 mbsf is likely driven by an increase in the abundance of diatoms and the frequency and occurrence of volcanic ash (Fig. 2B). This interval also coincides with increased hydrate concentrations based on porewater geochemistry calculations (Fig. 2C) (Collett et al., 2008; Ussler and Paull, 2001). (All grain size data collected for this study is available for download via https://edx.netl.doe.gov/ and also via JMPG.)

4.2. Petrographic analyses

Shipboard petrographic analyses reported by Collett et al. (2008) were integrated with SEM and BSE evaluations for seventeen NGHP-01 Site 17A sediment samples (Table 1) to further constrain compositional and textural relationships throughout the borehole. The handling and storage of these samples made them unsuitable for evaluating *in situ* sedimentary fabrics. The porewater samples were subjected to squeezing during pore water extraction, which significantly impacted the primary sedimentary fabric; the bulk sediment samples were significantly less disturbed, but since they were not collected with preservation of *in situ* sedimentary fabric in mind, they were also unsuitable for this purpose. However, SEM analyses allowed us to evaluate individual grain textures as well as the composition of primary particles, secondary precipitates, and alteration products. Visual observations were augmented with BSE-based composition measurements of select spot measurements or full field of view compositional maps.

Bulk sediment composition based on BSE and SEM image analyses was consistent with the lithostratigraphic Subunits described in Collett et al. (2008) (Fig. 5B). All ten bulk sediment samples (Table 1) contained a clay and nannofossil-rich matrix. Samples corresponding to the foraminifera-rich nannofossil ooze lithostratigraphic Subunit Ia, 7H-2 at 53 mbsf and 12H-1 at 100 mbsf, also contained foraminifera, volcanic glass shards, and based on visual evaluation and BSE analyses, trace amounts of SiO2, albite, and talc. Samples 23X-4 at 199 mbsf, 25X-1 at 214 mbsf, and 27X-1 at 233 mbsf were from the nannofossil-ooze lithostratigraphic Subunit Ib. Clay and biogenic nannofossil-rich matrix material are abundant in all three samples. BSE analysis was used to confirm the presence of clay and primary SiO_2, $CaCO_3$, orthoclase, and albite grains within the matrix material, as well as trace amounts of secondary silica and pyrite. Abundant authigenic carbonate grains were also observed in sample 27X-1. Samples 41X-2 at 349 mbsf, 50X-4 at 419 mbsf, 55X-4 at 465 mbsf, 56X-2 at 474 mbsf, and 73X-2 at 599 mbsf are diagnostic of the diatom-rich nannofossil ooze, Subunit Ic. In addition to the clay-biogenic ooze matrix, visual observation and BSE analyses confirmed the presence of primary SiO_2, $CaCO_3$, albite, and kaolinite grains, as well as secondary pyrite, silica, and carbonate precipitates throughout this interval.

SEM and BSE analyses were also used to evaluate the occurrence and form of volcanic glass shards and fragments at NGHP-01 Site 17A with particular attention paid to potential alteration products similar to those observed and documented by Spinelli et al. (2004, 2007), and White et al. (2011). In the bulk sediment samples, (Table 1) volcanic ash fragments were observed in trace to common amounts. Their physical condition in the bulk sediment samples was generally angular fragments and shards, showing very little sign of dissolution or secondary alteration. Volcanic ash fragments are very fine to fine silt grain size (Wentworth, 1922) based on both SEM based analysis and particle size analyses (Fig. 3). SEM samples prepared from porewater geochemistry subsamples correlated to volcanic ash layers (Table 1) contain higher abundances of ash, including relatively pristine pieces of pumice and glass shards (Fig. 5C), some of which exceeded coarse sand grain size and most of which fell within the medium silt to fine sand grain size range based on SEM and particle size analyses (Table 1). Secondary alteration of the volcanic ash was not widely observed in any of the SEM samples, other than secondary silica precipitation on some samples and some compositional alteration detected based on BSE analyses, which showed depletion of silica, aluminum and potassium along margins of volcanic ash fragments (SEM analyses of Site 17A samples available at https://edx.netl.doe.gov/).

Secondary mineralization observed via SEM and BSE analyses of the NGHP-01 Site 17A samples included pyrite, often in association with biogenic forms and iron sulfides in all seventeen samples. Occurrences of secondary silica at NGHP-01 Site 17A were observed in rare to trace amounts in lithostratigraphic Subunit Ic in samples 51X-3-HY, 53X-6-HY, 55X-2-HY, 55X-4, 56X-6, 56X-2-HY, and 66X-5-HY. The one exception was a trace observation of secondary silica precipitation over a foraminifera fragment in lithostratigraphic Subunit Ib. Secondary silica was almost always observed as framboidal or granular overgrowths on primary silica-rich forms such as quartz grains and volcanic ash fragments, however, it was also observed as overgrowths infrequently on biogenic forms such as diatoms and radiolarians. Secondary silica was also observed rarely as massive, banded overgrowths, and in one sample a silica bridge between a volcanic ash shard and matrix material was observed.

Secondary authigenic carbonate grains were observed in all samples analyzed from 27X-1 at 233 mbsf through 73X-2 at 599 mbsf (Table 1). The frequency of the secondary carbonate in these samples was common to abundant and most easily and often observed within the SEM epoxy mounting material (Fig. 7A and B) but were also observed upon close inspection within the sediment-rich portions of each SEM sample (Fig. 7C and D). Trace amounts of secondary carbonate mineral grains were also observed in sample

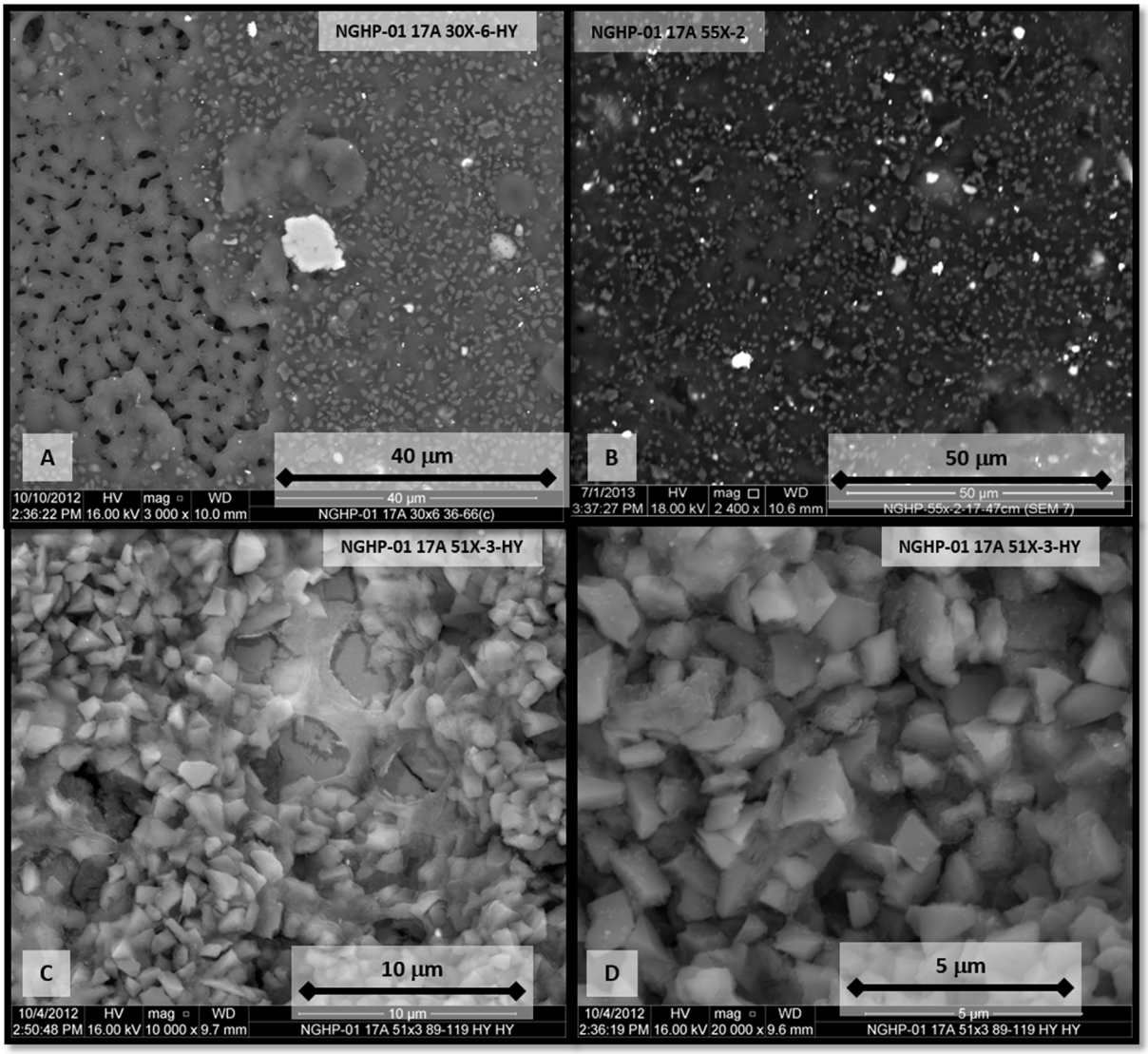

Figure 7. SEM images of secondary carbonate features in samples from NGHP-01 Site 17A. A) and B) large field of view showing carbonate rhombs as dominant visible form, and C) and D) carbonate rhomb-rich sections of a sample illustrating the uniform size and angular to sub-angular nature of these secondary precipitates.

12H-1. In all samples containing secondary carbonates the form and size of these grains was consistent, occurring as semi-euhedral, angular to rhombahedral grains, <1–3 µm in diameter (Fig. 7). SEM compositional analysis of these secondary carbonate grains was often impeded by their fine grain size and tendency to remain embedded in the epoxy mounting material. Where SEM compositional analysis was viable, the elemental analyses indicated that these grains were consistently comprised of magnesium, calcium carbonate minerals (Fig. 8) (All SEM analyses associated with this study of Site 17A samples available at https://edx.netl.doe.gov).

4.3. Silica, calcium, and magnesium activities and equilibrium at NGHP-01 Site 17A

The thermodynamic tendency of the three target minerals was studied by comparing the saturation curves with the ion activity products. Throughout the sediment column, dissolved silica is undersaturated with respect to pore water and thus should suffer from constant dissolution once it was buried in the sediments. On the contrary, calcite is close to saturation from 0 to 179 mbsf (or 5.5 to 8.9° C) and oversaturated with respect to the current pore water composition below 179 mbsf, almost to the depth where the anomalous porosity preservation, discussed in more detail below, is first observed (Fig. 2F).

5. Discussion

5.1. Hydrate occurrence versus lithologic parameters at NGHP-01 Site 17A

All three lithostratigraphic Subunits from Site 17A occur within the gas hydrate stability zone, with the base of gas hydrate stability occurring in Subunit Ic at ~605 mbsf (Fig. 2) (Collett et al., 2008). However, based on geophysical log estimates of hydrate saturation (Collett et al., 2008) and porewater chlorinity-based estimates using the methodology of Ussler and Paull (2001) (Fig. 2C), significant gas hydrate occurrences at Site 17A are almost entirely constrained to discrete intervals within Subunit Ic (Fig. 2A). Analysis of shipboard sediment core and geophysical logging datasets during the NGHIP-01 expedition documented a correlation between areas of higher gas hydrate concentration and the presence of volcanic ash (Figs. 2C and 3) (Figs. F13 and F43 in Collett et al., 2008). While

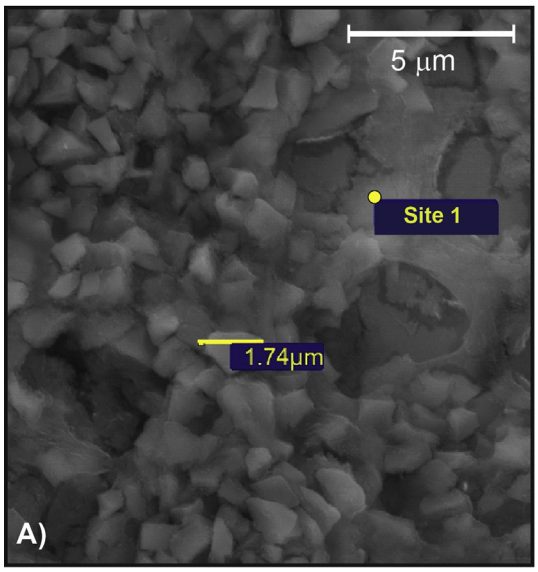

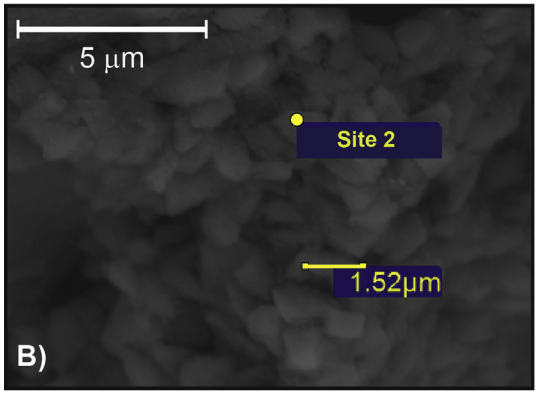

NGHP-01 17A 51x-3

Element	Weight%	Atomic%
C	26.54	37.36
O	44.21	46.72
Mg	0.12	0.08
Al	0.17	0.10
Si	19.44	11.70
S	0.11	0.06
Ca	9.42	3.97
Totals	100.00	

Site 1:
14.9 wt % SiO_2
37.7 wt % $CaCO_3$

Element	Weight%	Atomic%
C	63.20	73.90
O	23.44	20.57
Mg	0.20	0.12
Si	4.96	2.48
S	0.66	0.29
Ca	7.54	2.64
Totals	100.00	

Site 2:
58.3 wt % SiO_2
26.7 wt % $CaCO_3$

Figure 8. Compositional analysis at two carbonate-rich locations in NGHP-01 Site 17A 51X-3 sample. Spectrum analysis at site 1 (A) and site 2 (B) were taken on a carbonate grain overlying a siliceous radiolarian form. The normalized weight percent estimates at this site show the presence of SiO_2 and $CaCO_3$. The balance of the composition is related to epoxy and other trace minerals.

analysis of lithostratigraphic data from Site 17A shows that porous volcanic ash occurrences are common in two intervals within the borehole, in Subunit Ia from 0 to 165 mbsf, and in Subunit Ic between 365 and 600 mbsf (Figs. 2B and 3), gas hydrate occurrences were only observed in correlation with the ash layers in Subunit Ic which also had anomalously high porosities and likely enhanced permeabilities. Therefore, if gas hydrate occurrence was solely related to the presence of continuous, well-sorted, porous volcanic ash layers, the ashes observed in both Subunits Ia and Ic would contain elevated concentrations of gas hydrate. However, the gas hydrate saturated occurrences at Site 17A appear to be almost entirely correlated to continuous ash layers (Fig. 2B and C) in Subunit Ic (Cawthern et al., 2010; Collett et al., 2008). Organic geochemistry and pressure-core related datasets document the presence and availability of methane starting below the sulfate–-methane transition (SMT) zone at 25 mbsf through the base of the cored interval at NGHP-01 Site 17A (Collett et al., 2008) (Fig. 9). At NGHP-01 Site 17A methane concentrations directly below the SMT are probably below solubility limits required for gas hydrate stabilization (Claypool et al., 2006; Paull et al., 1996). However, methane was observed throughout the GHSZ, but significant gas hydrate accumulations were not documented until ~210 mbsf. This depth directly coincides with the onset of enhanced porosity (Fig. 2F). Quantitative estimates of methane concentrations at Site 17A are not available until deeper in the section (Fig. 9). However, controls on gas hydrate distribution and occurrence at Site 17A likely coincides with the presence of gas in excess of solubility coinciding with higher porosity reservoir lithofacies within the GHSZ.

The correlation between volcanic ash layers in Subunit Ic and hydrate occurrence is also constrained by thermal analysis of the cores. During shipboard operations, all sediment cores were subjected to infrared (IR) thermal camera scans, as the relationship between gas hydrate occurrence and cold thermal anomalies in sediment cores is well established by prior hydrate field efforts (Ford et al., 2003a,b; Long et al., 2010; Riedel et al., 2010; Trehu et al., 2004). Select sub-samples were also characterized via handheld IR imaging of porewater samples. Figure 3 illustrates, via IR images of two porewater sediment samples, the correlation between IR thermal anomalies and the occurrence of volcanic ash layers that was observed between 330 mbsf and the BSR at 605 mbsf at Site 17A (Collett et al., 2008). Closer evaluation of porewater geochemistry based estimates of gas hydrate concentrations relative to ash occurrences (Fig. 2C) and select hand-held IR images (Fig. 3) supports the first-order relationship between higher hydrate concentrations and volcanic ash-rich beds. Some porewater geochemistry samples that contained visible IR anomalies and/or ash beds were selectively characterized, so that there are separate porewater geochemistry measurements for the bulk sediment versus the ash-rich portions of the sample (e.g. Fig. 3) (Collett et al., 2008). Thus, for Site 17A sediment cores the relationship between gas hydrate occurrence and volcanic ash layers is

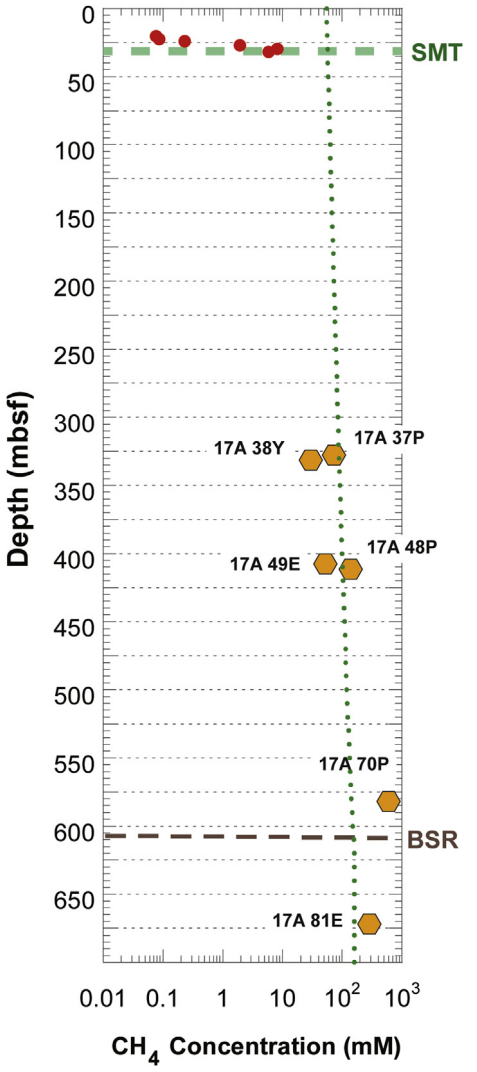

Figure 9. Using data from Collett et al. (2008), red circles are headspace methane gas concentration (mM) versus depth from NGHP-01 Site 17A to the base of the SMT. Below this depth methane concentration data is shown in orange based on pressure core measurements. The theoretical methane solubility is shown as green dashed line from Collett et al. (2008). (For interpretation of the references to color in this figure legend, the reader is referred to the web version of this article.)

demonstrated based on correlation of core IR scans, lithostratigraphic descriptions, (see Fig. F11 Collett et al., 2008), and pore-water geochemistry anomalies (Fig. 4 and Figs. F25 and F26 from Collett et al., 2008).

The particle size analyses conducted in this study help to further characterize and constrain the nature of the lithology-hydrate occurrence relationships at Site 17A. As illustrated in Figures 3–5, volcanic ash-rich samples largely occurred with median grain size fractions of coarse-silt to medium-sand size, and distributions that were tight or bimodal (Fig. 5) indicating moderate to well sorting. In contrast, the bulk sediment profiles averaged consistently in the fine-silt fraction both adjacent to (Figs. 3 and 5) and throughout (Fig. 4) the Site 17A profile and display broader distributions (Figs. 4 and 5) indicating a wider range of grain sizes than the ash-rich intervals. The correlation between grain size, gas hydrate saturation, physical properties, and lithology data at Site 17A (Fig. 2) confirms that hydrate occurrences appear to be related to coarser-grained, more well sorted ash-rich lithofacies in Subunit Ic.

This relationship between gas hydrate abundance and discrete reservoirs comprised of coarse-grained media such as volcanic ash or clastic sand layers is documented by previous studies (e.g. Bahk et al., 2014, 2013; Boswell et al., 2012; Collett et al., 2012; Malinverno et al., 2008; Torres et al., 2008; Uchida et al., 2009). Generally, in these systems the hydrate-host strata is both coarser grained and more well-sorted than the bounding bulk lithofacies. While it is commonly observed that the upper portion of the gas hydrate stability zone in subsurface systems is devoid of significant or any gas hydrate occurrences, the lack of hydrate occurrences at Site 17A is strongly correlated with the shift in porosity from ~175 to ~210 mbsf (Fig. 2C and F). Gas hydrate was observed in discrete samples at significant concentrations throughout the sedimentary sequence below this interval, but not above it. This indicates that more parameters are at play in the distribution of gas hydrate in the sedimentary sequence at Site 17A than just the availability of methane and the presence or absence of coarser-grained sedimentary layers to serve as suitable reservoir lithofacies. The lack of hydrates in coarser-grained volcanic-ash rich beds in the upper half of Subunit 1b and Subunit 1a at Site 17A appears related to grain-scale phenomenon documented in this study. In particular, the decrease in porosity throughout this interval, which may have restricted permeability enough to impede methane migration at quantities sufficient enough to support hydrate formation in the shallower half of Site 17A. not needed.

5.2. Anomalous porosity profile at NGHP-01 Site 17A

Physical properties measurements including porosity were collected on 485 samples from NGHP-01 Site 17A (Collett et al., 2008). Examination of the sediment core porosity data for Site 17A shows an anomalous porosity profile (Fig. 2F) with depth. In particular, throughout Subunit Ic, the actual porosity profile for bulk sediment and ash-rich samples is anomalously high relative to the expected porosity-depth profile for a calcareous ooze (Hamilton, 1976). In calcareous-rich sediments, such as those at NGHP-01 Site 17A, the expected fractional porosity (ϕ) versus depth relationship can generally be described by the general regression equation:

$$\phi = 0.72 - 0.987(D) + 0.830\left(D^2\right) \quad (1)$$

where D = depth in km (see Hamilton, 1976, Fig. 1 and Table 1), such that ϕ decreases with depth from a near surface porosity of ~70% until lithification at about 50% ϕ (Fig. 2F).

The porosity profile at Site 17A was compared against other calcareous-rich sediment profiles from around the Indian Ocean using data from eleven boreholes drilled by DSDP and ODP in the Indian Ocean (Figs. 1B and 10). From 0 to ~200 mbsf the Site 17A porosity record is consistent with these calcareous-ooze sediment borehole records. However, the porosity increase and preservation from 200 to 685 mbsf at Site 17A (Fig. 2F) is not visible in any other record (Fig. 10) and is anomalous relative to the predicted porosity versus depth curve for a calcareous-rich ooze (Fig. 2F) (Hamilton, 1976). ODP Leg-123 Site 765 does contain porosity anomalies in its deeper record, but the overall porosity trend maintains the expected trend of decreasing porosity with increasing depth per Hamilton (1976). Thus, the anomalously high porosity at depth in the core from Site 17A is unique amongst these records (Fig. 10).

The measured porosity at Site 17A is initially consistent with the expected porosity versus depth curve for calcareous-rich sediments (Fig. 2F), starting with near seafloor porosities in the upper 70%'s and decreasing generally exponentially with depth to 47% at 200 mbsf where the porosity values reversed their trend (Fig. 2F). This depth corresponds to an increase in biogenic silica (Fig. 2D), and as expected, siliceous sediments normally have higher porosity

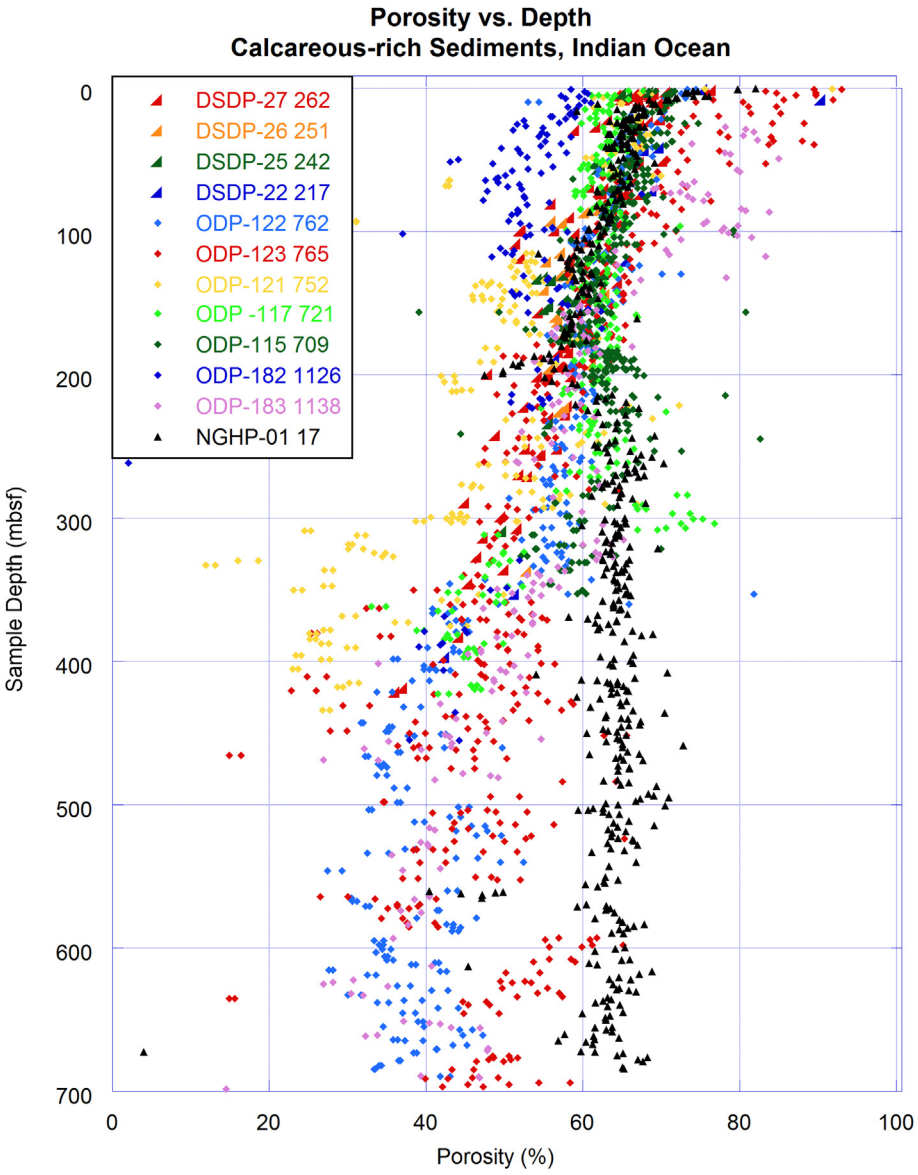

Figure 10. Summary plot illustrating porosity versus depth measurements for calcareous-rich sediment boreholes from DSDP and ODP records from across the Indian Ocean compared against sediment porosity measurements for NGHP-01 Site 17A (Collett et al., 2008).

(Hamilton, 1976). However, silicate ooze sediments are generally expected to decrease in porosity with depth (Hamilton, 1976). Secondary opal-CT precipitation as a result of volcanic ash alteration in a borehole from the Nankai Trough is documented to have resulted in enhanced porosity preservation in those marine sediments (Spinelli et al., 2004, 2007; White et al., 2011). SEM analyses of samples at Site 17A, however, show no evidence of significant opal-CT precipitation. In addition, thermodynamic saturation analyses of 17A porewater samples confirm dissolved silica is unavailable for precipitation in this system (Fig. 6). (For interpretation of the references to color in this figure legend, the reader is referred to the web version of this article.)

5.3. Role of micro-crystalline secondary carbonates at Site 17A

The thermodynamic behavior of three target minerals was assessed in this study by comparing saturation curves with the ion activity products (Fig. 6). Throughout the sediment column, amorphous silica is undersaturated with respect to the current pore water composition (Fig. 6A) and thus should experience constant dissolution within the sediment column throughout Site 17A. In Subunits Ia and Ib, calcite is close to saturation (Fig. 6B) from 0 to 179 mbsf (or 5.5–8.9 °C) but becomes oversaturated with respect to pore water composition below 179 mbsf. This depth generally coincides with the depth where the anomalous porosity trend initiates (Fig. 2F). Although oversaturation does not guarantee mineral precipitation, it suggests that calcite is thermodynamically permitted to form under the current environment and implies the likelihood of secondary carbonate precipitation in the section where porosity preservation at Site 17A is observed. This analysis also suggests that the precipitation/dissolution of calcite maybe sensitive to the changes in pore water composition and the temperature regime as its ion activity products are closer to saturation.

SEM and grain size analyses of samples throughout the sediment column at Site 17A (Table 1) corroborate the prediction of carbonate precipitation initiating around 200 mbsf. SEM samples evaluated within Subunit Ic contained visibly significant amounts of fine-grained, angular to sub-angular carbonate rhombs (Fig. 7).

SEM-based compositional analyses of these grains documented the presence of calcium and magnesium-rich carbonates. Throughout all of the samples assessed, the grain size of these carbonate grains, based on SEM analysis, was uniformly and consistently within the 1–5 μm size distribution.

This grain size fraction coincides with the minor peak on the ash grain size bimodal distributions for all ash-rich samples that were assessed (Figs. 3 and 5A). In addition, the bulk sediment grain size distributions show an increase in the volume of grains within the 1–5 μm size fraction starting around 160 mbsf. While these grains are generally in the fine-silt size fraction, their consistent grain size and angular shape would contribute to enhanced porosity and permeability in the volcanic ash layers (Brayshaw et al., 1996; Hamilton, 1976; McKinley et al., 2011; Nelson, 1994; Spinelli et al., 2007). Thus, based on the geochemical activity, SEM and grain size evidence from Site 17A, the enhanced porosity observed in Subunit Ic appears to be correlated with the precipitation of fine-grained authigenic carbonate rhombs. In addition, the volume of authigenic carbonate crystals within each sample was substantial enough to skew the grain size distributions for both volcanic ash-rich and bulk sediment samples throughout the anomalous porosity interval at Site 17A.

5.4. Porosity preservation, permeability, and gas hydrate saturation

Secondary alteration of *in situ* marine sediments resulting in porosity preservation was demonstrated by Spinelli et al. (2007) and White et al. (2011). In these studies, significant and clearly visible alteration of volcanic glass fragments led to fine-scale secondary silica precipitation features that resulted in sediment stabilization and porosity preservation in the subsurface, offshore Nankai trough, Japan. However, SEM, grain size, and geochemical analyses of samples from Site 17A show that at this location pervasive authigenic carbonate precipitation is likely responsible for the anomalous porosity preservation at this site.

The bulk sediment distribution curves (Figs. 3 and 5A) are generally centered around the 1–5 μm size fraction and present a broader distribution profile than the ashes, indicating they are less well-sorted, and finer grained than the volcanic ash-rich samples. Upon close examination, many of the bulk sediment and ash-rich samples appear skewed to varying degrees around the 1–5 μm interval, with several of the ash-rich samples showing a less pronounced, but visibly present bi-modal grain size distribution (Fig. 5A). This bimodal distribution was not observed in another system where hydrate concentration in coarser grained lithofacies was compared to grain size distributions of the bulk sediment profiles (Bahk et al., 2014, 2013). At Site 17A the SEM evidence of secondary carbonate crystals of the 1–5 micron grain size fraction supports the conclusion that they comprise a significant portion of this size fraction in the anomalous porosity section of Site 17A.

The occurrence of gas hydrate at Site 17A adheres to prior observations that require the presence of methane and appropriate reservoir lithofacies to accumulate gas hydrate in marine sediments. In addition, this study documents the importance of permeability tied to enhanced porosity controlling the concentration of hydrate in the coarse grained, porous volcanic ash layers. *In situ* permeability measurements were not collected at Site 17A, however, general relationships between grain size, grain shape, sorting, porosity and permeability are well established from field and laboratory measurements and offer insights into the system at Site 17A (e.g. Brayshaw et al., 1996; McKinley et al., 2011; Nelson, 1994). Factors that affect permeability include pore size, grain size distribution, grain shape, packing of grains, and the type and amount of secondary porosity, and porosity reduction due to

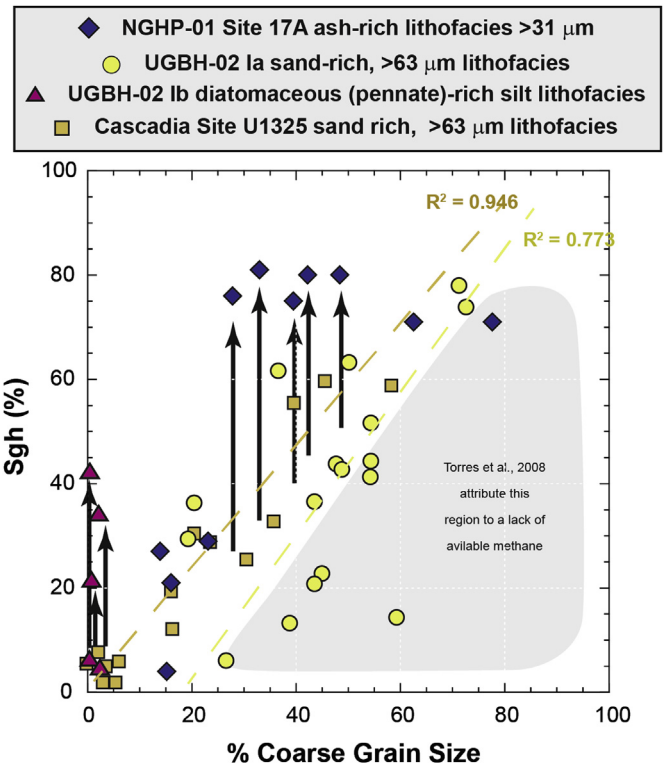

Figure 11. Plot comparing gas hydrate saturation versus % coarse grains (>31 μm for NGHP-01 Site 17A and >63 μm for UBGH-02 and Cascadia samples) in volcanic ash-rich layers from NGHP-01 Site 17A, sand-rich layers from Cascadia Margin U1325 (Torres et al., 2008) and two lithofacies types, sand-rich layers (Ia) and diatomaceous-rich silt layers (Ib) from the UBGH-02 in the East Sea (Bahk et al., 2013). Black arrows indicate samples that appear to have high gas hydrate saturations relative to the volume of coarse grains present. (For interpretation of the references to color in this figure legend, the reader is referred to the web version of this article.)

secondary mineral precipitation. Permeability is strongly related to pore throat size, which is in turn tied to sorting and the median grain size of the sediment system. The coarser the grain size and more well sorted the sediment the larger the pore throat sizes, and by extension, the effective permeability for a given lithology (Bryant and Blunt, 1992; Evans and Bryant, 1994). At Site 17A, the grain size distribution, grain shape and secondary porosity indicate that pore throat sizes in both the bulk and volcanic ash-rich sediment within the anomalous porosity interval would be enhanced as a result of the porosity preservation in Subunit Ic.

In addition to the effects of grain size and sorting, compaction with depth plays a significant role in permeability. Compaction-related permeability is strongly tied to porosity, so as porosity is reduced permeability declines as well (Bryant and Blunt, 1992; Evans and Bryant, 1994; Mckinley et al., 2011). Therefore, at Site 17A the portion of the borehole that experienced secondary porosity preservation as a result of the authigenic carbonate precipitation likely benefitted from enhanced permeability. The highest permeabilities are likely associated with the coarser grained and more well-sorted volcanic ash layers, but the finer grained bulk sediment profile would also see enhanced permeabilities. As a result, migration of methane, which was pervasive throughout Site 17A (Fig. 9), into the coarser grained volcanic ash layers would be supported by the enhanced porosity and permeability in Subunit Ic.

Other recent studies focused on constraining the detailed relationship between the sediment framework and gas hydrate occurrence have also identified fine-scale controls on hydrate distribution (Bahk et al., 2014, 2013; Rose et al., 2011; Winters

et al., 2011) beyond the presence or absence of coarse-grained, porous beds (Malinverno, 2010). Torres et al. (2008) and Bahk et al. (2013) demonstrated a correlation between sand-rich lithofacies and increased gas hydrate saturation in those systems (Fig. 11). While volcanic ash layers with more than 30% grains >31 μm at Site 17A contained high concentrations of gas hydrate, they do not always show the same correlation between increasing gas hydrate saturation and increasing percentage of coarse grains (Fig. 11). Similarly, diatomaceous-rich silt samples from UBGH-02, while overall finer grained, have higher gas hydrate saturations than expected from the gas hydrate saturation versus grain size trends (Fig. 11). Based on our results, we suggest that these higher gas hydrate saturations are driven by increased pore space and pore throat connectivity created by the presence of angular and/or low sphericity grains. Thus grain shapes, such as the angular authigenic carbonate rhombs in Site 17A Subunit Ic or the low-sphericity pennate diatoms from UBGH-02 9 (Bahk et al., 2013), can contribute to conditions favorable for higher gas hydrate accumulations.

Free-gas occurrences have been documented in many marine sediment systems coinciding with the base of the GHSZ. Paull et al. (1994) and others have shown that free-gas can occur widely throughout the GHSZ. Studies by Clennell et al. (1999) and Henry et al. (1999) document the effect of pore space and other host-sediment effects on the stability and formation of gas hydrate. Specifically, these studies illustrate that hydrate growth is inhibited in finer grained sediments as a result of thermodynamic constraints related to the small pore spaces and chemistry of the system. In addition, Clennell et al. (1999) and Henry et al.'s (1999) studies indicate that more closed, lower permeability systems are less likely to support concentrated hydrate formation and growth. Moreover, they conclude that low or restricted water content and increased consolidation of the host sediment framework inhibit hydrate growth. Thus, at Site 17A, the enhanced permeability conditions in the bulk sediment column, but particularly in the more porous and coarser grained ash layers would support sustained flow through the system of both methane and pore-water which are necessary to support the development of concentrated hydrate accumulations.

6. Conclusions

A suite of sediment composition, physical and geochemical properties data provided evidence that secondary mineralization results in porosity preservation and enhanced permeability in sediments from NGHP-01 Site 17A. Such secondary minerals thus lead to conditions favorable to concentrated hydrate accumulation in volcanic ash layers below 200 mbsf at this site and demonstrate the importance of grain-scale subsurface heterogeneities in controlling the occurrence and distribution of concentrated gas hydrate accumulations in marine sediments. In addition, this study documents the importance that increased permeability and enhanced porosity play in supporting gas concentrations sufficient to support hydrate formation and offer insights into what may control the occurrence and distribution of gas hydrate in other sedimentary settings.

The shallow half of Site 17A shows a typical porosity versus depth profile for marine calcareous sediments, which is in contrast to the anomalous porosity profile observed in the deeper portion of Site 17A. In Subunit Ia the surrounding bulk sediment framework had little to no visible authigenic carbonate grains, was less porous and likely less permeable than sediments in the deeper stratigraphy. Thus, it is likely that low permeability hindered methane migration into the volcanic ash-rich layers in the shallow section, contributing to the lack of hydrate in this interval. Below 175mbsf, however, porosity throughout the section is anomalous and enhanced relative to the predicted porosity versus depth relationship. Collectively, downhole grain size, SEM analyses, and porewater based mineral saturation and ion activity products, a reveal the importance of authigenic carbonate microcrystals that form starting around 179 mbsf. While these carbonate grains are relatively fine grain size, 1–5 μm, their consistent grain size and shape, as well as their abundant presence within the anomalous porosity interval at Site 17A play a significant role in maintaining pore volume and enhanced pore throat connectivity at this site.

The physical property, sedimentology, and geochemical data from Site 17A demonstrate a relationship between anomalous porosity preservation, secondary micro-carbonate precipitation, and the likelihood of enhanced permeability throughout the deeper half of the Site 17A system that leads to the observed preferential gas hydrate accumulation in coarser grained, porous volcanic ash layers. This study shows that gas hydrate distribution responds to a complex set of parameters that represent the interplay between the geometry of porous-permeable strata and a natural gas source. The grain scale relationships documented at Site 17A likely have implications for understanding what controls the occurrence and distribution of hydrate in other sedimentary settings. Future work involving physical and geochemical modeling of the porosity, permeability, and gas hydrate accumulation at Site 17A could provide further insights on the controls of gas hydrate occurrence under a variety of scenarios.

Acknowledgments

The author(s) wish to thank those that contributed to the success of the National Gas Hydrate Program Expedition 01 (NGHP01). NGHP01 was planned and managed through collaboration between the Directorate General of Hydrocarbons (DGH) under the Ministry of Petroleum and Natural Gas (India), the U.S. Geological Survey (USGS), and the Consortium for Scientific Methane Hydrate Investigations (CSMHI) led by Overseas Drilling Limited (ODL) and FUGRO McClelland Marine Geosciences (FUGRO). The platform for the drilling operation was the research drill ship JOIDES Resolution, operated by ODL. Much of the drilling/coring equipment used was provided by the Integrated Ocean Drilling Program (IODP) through a loan agreement with the US National Science Foundation. Wireline pressure coring systems and supporting laboratories were provided by IODP/Texas A&M University (TAMU), FUGRO, USGS, U.S. Department of Energy (USDOE) and HYACINTH/GeoTek. Downhole logging operational and technical support was provided by Lamont-Doherty Earth Observatory (LDEO) of Columbia University. The financial support for the NGHP01, from the Oil Industry Development Board, Oil and Natural Gas Corporation Ltd., GAIL (India) Ltd. and Oil India Ltd. is gratefully acknowledged. We also acknowledge the support extended by all the participating organizations of the NGHP: MoP&NG, DGH, ONGC, GAIL, OIL, NIO, NIOT, and RIL.

In addition we wish to thank, at the U.S. Department of Energy's National Energy Technology Lab in Albany, Oregon, Lars Paulson for assistance with particle size analyses, Circe Verba and Audrey Oldenkamp for assistance with SEM sample preparation and analyses, and Jennifer Bauer for assistance with map development. We thank Steven Phillips at UNH for discussions and coordination relative to the interpolated plotting of grain size data. At Oregon State University we thank Jonathan Yang for discussions in relation to porewater geochemistry data and analyses. We thank William Winters with the U.S. Geological Survey for discussions about and use of the field generated physical properties datasets for Site 17A.

References

Bahk, J.-J., Um, I.-K., Holland, M., 2011. Core lithologies and their constraints on gas-hydrate occurrence in the East Sea, offshore Korea; results from the site UBGH1-9. Mar. Petrol. Geol. 28, 1943–1952.

Bahk, J.J., Kim, D., Chun, J., Son, B., Kim, J., Ryu, B., Torres, M., Schultheiss, P., Ryu, B., Riedel, M., 2014. Gas hydrate occurrences and their relation to host sediment properties: results from second Ulleung Basin gas hydrate drilling expedition, East Sea (Korea). J. Mar. Petrol. Geol. 19 (submitted for publication).

Bahk, J.J., Kim, D.H., Chun, J.H., Son, B.K., Kim, J.H., Ryu, B.J., Torres, M.E., Riedel, M., Schultheiss, P., 2013. Gas hydrate occurrences and their relation to host sediment properties: results from second Ulleung Basin Gas hydrate drilling expedition, east sea. Mar. Petrol. Geol. 47, 21–29.

Bastia, R., Radhakrishna, M., 2012. Basin Evolution and Petroleum Prospectivity of the Continental Margins of India. Access Online via Elsevier.

Boswell, R., Collett, T., Anderson, B., Hunter, R., 2011. Thematic set on Scientific results of the Mount Elbert gas hydrate stratigraphic test well, Alaska North Slope. pp. 279–607.

Boswell, R., Collett, T.S., Frye, M., Shedd, W., Mcconnell, D.R., Shelander, D., 2012. Subsurface gas hydrates in the northern Gulf of Mexico. Mar. Petrol. Geol. 34, 4–30.

Brayshaw, A.C., Davies, G.W., Corbett, P.W.M., 1996. Depositional controls on primary permeability and porosity at the bedform scale in fluvial reservoir sandstones. Adv. Fluvial Dyn. Stratigr., 373–394.

Bryant, S., Blunt, M., 1992. Prediction of relative permeability in simple porous media. Phys. Rev. A 46, 2004.

Cawthern, T., Johnson, J., Bryce, J., Bilcert-toft, J., Flores, J., 2010. A ~9.4 Ma ash record from the Andaman Accretionary Wedge: petrochemical implications for arc evolution. American Geophysical Union Fall Meeting. San Francisco, CA.

Cawthern, T., Johnson, J., Giosan, L., Flores, J.A., Rose, K., 2014. a mid-Late Pliocene biogenic silica Crash in the andaman sea: potential teleconnections to the Pacific and Atlantic Oceans. J. Mar. Petrol. Geol. (in this issue).

Chakraborty, P.P., Sharma, R., Roy, S.B., 2013. A key role played by hydrocarbon industry in Indian economy and the road ahead. Int. J. Adv. Earth Environ. Sci. 1.

Claypool, G.E., Milkov, A.V., Lee, Y.-J., Torres, M.E., Borowski, W.S., Tomaru, H., 2006. Microbial methane generation and gas transport in shallow sediments of an accretionary complex, southern Hydrate Ridge (ODP Leg 204), offshore Oregon, USA. In: Tréhu, A.M., Bohrmann, G., Torres, M.E., Colwell, F.S. (Eds.), Proc. ODP, Sci. Results, vol. 204. Ocean Drilling Program, College Station, TX, pp. 1–52. http://dx.doi.org/10.2973/odp.proc.sr.204.113.2006.

Clennell, M.B., Hovland, M., Booth, J.S., Henry, P., Winters, W.J., 1999. Formation of natural gas hydrates in marine sediments: 1. Conceptual model of gas hydrate growth conditioned by host sediment properties. J. Geophys. Res. Solid Earth 104, 22985–23003 (1978–2012).

Cochran, J.R., 2010. Morphology and tectonics of the Andaman Forearc, northeastern Indian Ocean. Geophys. J. Int. 182, 631–651.

Collett, T.S., Lee, M.W., Agena, W.F., Miller, J.J., Lewis, K.A., Zyrianova, M.V., Boswell, R., Inks, T.L., 2011. Permafrost-associated natural gas hydrate occurrences on the Alaska North Slope. Mar. Petrol. Geol. 28, 279–294.

Collett, T.S., Lee, M.W., Zyrianova, M.V., Mrozewski, S.A., Guerin, G., Cook, A.E., Goldberg, D.S., 2012. Gulf of Mexico Gas Hydrate Joint Industry Project Leg II logging-while-drilling data acquisition and analysis. Mar. Petrol. Geol. 34, 41–61.

Collett, T.S., Reidel, M., Cochran, J., Boswell, R., Presley, J., Kumar, P., Sathe, A., Sethi, A., Lall, M., Sibal, V., Party, N.-S., 2008. Indian National Gas Hydrate Program Expedition 01 Initial Reports.

Cook, A.E., Malinverno, A., 2013. Short migration of methane into a gas hydrate-bearing sand layer at Walker Ridge, Gulf of Mexico. Geochem. Geophys. Geosyst. 14, 283–291.

Curray, J.R., 1979. Eastern Indian outer continental margin and its relationship to the Bay of Bengal. Int. Union Geodesy Geophys. Gen. Assem., 4.8.

Curray, J.R., 2005. Tectonics and history of the Andaman Sea region. J. Asian Earth Sci. 25, 187–232.

Curray, J.R., Moore, D.G., 1974. Sedimentary and tectonic processes in the Bengal deep-sea fan and geosyncline. pp. 617–627.

DeMaster, D.J., 1981. The supply and accumulation of silica in the marine environment. Geochim. Cosmochim. Acta 45, 1715–1732.

Evans, C.A., Bryant, S.L., 1994. Analysis of permeability controls: a new approach. Clay Miner. 29, 10.

Flores, J.A., Johnson, J.E., Mejia-molina, A.E., Álvarez, M.C., Sierro, F.J., Singh, S.D., Mahanti, S., Giosan, L., 2014. Sedimentation rates from calcareous nannofossil and planktonic foraminifera biostratigraphy in the Andaman Sea, northern Bay of Bengal, and Eastern Arabian Sea. Mar. Petrol. Geol. 58, 425–437.

Folk, R.L., 1966. A review of grain-size parameters. Sedimentology 6, 73–93.

Ford, K.H., Naehr, T.H., Skilbeck, C.G., the Leg 201 Scientific Party, 2003a. The use of infrared thermal imaging to identify gas hydrate in sediment cores. pp. 1–20.

Ford, K.H., Naehr, T.H.. Skilbeck, C.G, 2003b. The Leg 201 Scientific Party, 2003. The use of infrared thermal imaging to identify gas hydrate in sediment cores. pp. 1–20.

Frye, M., 2008. Preliminary evaluation of in-place gas hydrate resources: Gulf of Mexico outer continental shelf. pp. 136.

Frye, M., Shedd, W., Schuenemeyer, J., 2013. Gas hydrate resource assessment Atlantic outer Continental Shelf. pp. 57.

Gieskes, J.M., Gamo, T.,, Brumsack, H., 1991. Chemical Methods for Interstitial Water Analysis Aboard JOIDES Resolution. Ocean Drilling Program, Texas A & M University.

Goldstein, J.I., Newbury, D.E., Echlin, P., Joy, D.C., Romig, A.D., Lyman, C.E., Fiori, C., Lifshin, E., 1997. Scanning electron microscopy and x-ray microanalysis.

Hamilton, E.L., 1976. Variations of density and porosity with depth in deep-sea sediments. J. Sediment. Res. 46, 280–300.

Henry, P., Thomas, M., Clennell, M.B., 1999. Formation of natural gas hydrates in marine sediments: 2. Thermodynamic calculations of stability conditions in porous sediments. J. Geophys. Res. Solid Earth 104, 23005–23022 (1978–2012).

Johnson, A.H., 2011. Global resource potential of gas hydrate–a NEW CALCULATION. Nat. Gas Oil 304, 285–4541.

Johnson, J.W., Oelkers, E.H., Helgeson, H.C., 1992. SUPCRT92: a software package for calculating the standard molal thermodynamic properties of minerals, gases, aqueous species, and reactions from 1 to 5000 bar and 0 to 1000 C. Comput. Geosci. 18, 899–947.

Johnson, J., Phillips, S., Miranda, E., Giosan, L., Rose, K., 2014. Long-term variability of carbon and nitrogen in the Bay of Bengal and Arabian Sea. J. Mar. Petrol. Geol. (in this volume).

Kneafsey, T.J., Seol, Y., Moridis, G.J., Tomutsa, L., Freifeld, B.M., 2009. Laboratory measurements on core-scale sediment and hydrate samples to predict reservoir behavior. AAPG Memoir 89, 125.

Krishna, M.R., Sanu, T.D., 2002. Shallow seismicity, stress distribution and crustal deformation pattern in the Andaman-West Sunda arc and Andaman Sea, northeastern Indian Ocean. J. Seismol. 6, 25–41.

Kvenvolden, K.A., 1988. Methane hydrate—a major reservoir of carbon in the shallow geosphere? Chem. Geol. 71, 41–51.

Kvenvolden, K.A., Lorenson, T.D., 2000. The global occurrence of natural gas hydrate.

Lee, M.W., Collett, T.S., 2011. In-situ gas hydrate hydrate saturation estimated from various well logs at the Mount Elbert Gas Hydrate Stratigraphic Test Well, Alaska North Slope. Mar. Petrol. Geol. 28, 439–449.

Lee, M.W., Collett, T.S., Lewis, K.A., 2012. Anisotropic models to account for large borehole washouts to estimate gas hydrate saturations in the Gulf of Mexico Gas Hydrate Joint Industry Project Leg II Alaminos Canyon 21 B Well. Mar. Petrol. Geol. 34, 85–95.

Long, P., Holland, M., Schultheiss, P., Riedel, M., Weinberger, J., Tréhu, A., Schaef, H., 2010. Infrared imaging of gas-hydrate-bearing cores: state of the art and future prospects. In: Geophysical characterization of gas hydrates: SEG geophysical developments series, pp. 217–231.

Lu, H., Kawasaki, T., Ukita, T., Moudrakovski, I., Fujii, T., Noguchi, S., Shimada, T., Nakamizu, M., Ripmeester, J., Ratcliffe, C., 2011. Particle size effect on the saturation of methane hydrate in sediments – constrained from experimental results. Mar. Petrol. Geol. 28, 1801–1805.

MacDonald, G.J., 1990. The future of methane as an energy resource. Annu. Rev. Energy 15, 53–83.

Malinverno, A., 2010. Marine gas hydrates in thin sand layers that soak up microbial methane. Earth Planet. Sci. Lett. 292, 399–408.

Malinverno, A., Kastner, M., Torres, M.E., Wortmann, U.G., 2008. Gas hydrate occurrence from pore water chlorinity and downhole logs in a transect across the northern Cascadia margin (Integrated Ocean Drilling Program Expedition 311). J. Geophys. Res. 113. @CitationB08103–@CitationB08103.

Manheim, F.T., Sayles, F.L., 1974. Composition and origin of interstitial waters of marine sediments, based on deep sea drill cores. In: The Sea: Ideas and Observations on Progress in the Study of the Seas, p. 5.

Max, M.D., Johnson, A.H., Dillon, W.P., 2006. Economic Geology of Natural Gas Hydrate. Springer.

McKinley, J.M., Atkinson, P.M., Lloyd, C.D., Ruffell, A.H., Worden, R.H., 2011. How porosity and permeability vary spatially with grain size, sorting, cement volume, and mineral dissolution in fluvial Triassic sandstones: the value of geostatistics and local regression. J. Sediment. Res. 81, 844–858.

Milkov, A.V., 2004. Global estimates of hydrate-bound gas in marine sediments: how much is really out there? Earth-Sci. Rev. 66, 183–197.

Mohan, K., Vinod Dangwal, S.G., Sengupta, S., Desai, A.G., 2006. Andaman Basin – A Future Exploration Target. The Leading Edge, pp. 964–967.

Mortlock, R.A., Froelich, P.N., 1989. A simple method for the rapid determination of biogenic opal in pelagic marine sediments. Deep Sea Res. Part A Oceanogr. Res. Pap. 36, 1415–1426.

Nelson, P.H., 1994. Permeability–porosity relationships in sedimentary rocks. Log Anal. 35, 38.

Pal, T., Chakraborty, P.P., Gupta, T.D., Singh, C.D., 2003. Geodynamic evolution of the outer-arc-forearc belt in the Andaman Islands, the central part of the Burma-Java subduction complex. Geol. Mag. 140, 289–307.

Paull, C.K., Matsumoto, R., Wallace, P., 1996. Leg 164 Science Party, Proceedings of the Ocean Drilling Program, Initial Reports, 164, Ocean Drill. Program, College Station, Tex.

Paull, C.K., Ussler, W., Borowski, W.S., 1994. Sources of biogenic methane to form Marine Gas hydrates – in-situ production or upward migration. In: International Conference on Natural Gas Hydrates, vol. 715, pp. 392–409.

Phillips, S.C., Johnson, J.E., Miranda, E., Disenhof, C., 2011. Improving CHN measurements in carbonate-rich marine sediments. Limnol. Oceanogr. Methods 9, 194–203.

Raju, K.A.K., Murty, G.P.S., Amarnath, D., Kumar, M.L.M., 2007. The West Andaman Fault and its influence on the the aftershock pattern of the recent megathrust earthquakes in the Andaman-Sumatra region. Geophys. Res. Lett. 34. @L03305–@L03305.

Riedel, M., Collett, T.S., Malone, M.J., The Expedition 311 Scientists, 2010. DC (Integrated Ocean Drilling Program Management International, Inc.). Proc. IODP.

Integrated Ocean Drilling Program Management International, Inc., Washington, DC. In: http://dx.doi.org/10.2204/iodp.proc.311.213.2010, 311.
Rodolfo, K.S., 1969. Bathymetry and Marine Geology of Andaman Basin, and tectonic implications for Southeast Asia. Geol. Soc. Am. Bull. 80, 1203.
Rose, K., Boswell, R., Collett, T., 2011. Mount Elbert gas hydrate stratigraphic test well, Alaska North Slope; coring operations, core sedimentology, and lithostratigraphy. Mar. Petrol. Geol. 28, 311–331.
Shankar, U., Riedel, M., 2013. Heat flow and gas hydrate saturation estimates from Andaman Sea, India. Mar. Petrol. Geol. 43, 434–449.
Sloan, E.D., Koh, C.A., 2008. Clathrate Hydrates of Natural Gases. Taylor & Francis/CRC Press.
Solomon, E.A., Kastner, M., Torres, M., Spivak, A., 2014. Pore fluid geochemistry and gas hydrate distribution in the Krishna-Godavari basin cored during NGHP Expedition 01. J. Mar. Petrol. Geol. (in this issue).
Sperazza, M., Moore, J.N., Hendrix, M.S., 2004. High-resolution particle size analysis of naturally occurring very fine-grained sediment through laser diffractometry. J. Sediment. Res. 74, 736–743.
Spinelli, G.A., Mozley, P., Underwood, M., Tobin, H., 2004. Opal diagenesis and sediment properties in the Nankai Trough, Japan. Eos, Trans. Am. Geophys. Union 85. @AbstractT41E-1256.
Spinelli, G.A., Mozley, P.S., Tobin, H.J., Underwood, M.B., Hoffman, N.W., Bellew, G.M., 2007. Diagenesis, sediment strength, and pore collapse in sediment approaching the Nankai Trough subduction zone. Geol. Soc. Am. Bull. 119, 377–390.
Steefel, C.I., 2009. CrunchFlow software for modeling multicomponent reactive flow and transport. User's manual. Earth Sciences Division. Lawrence Berkeley, National Laboratory, Berkeley, CA. October, 12–91.
Strickland, J.D., Parsons, T.R., 1972. Practical handbook of seawater analysis. Bull. Fish. Res. Board Canada 167, 311.
Terry, R.D., Chilingar, G.V., 1955. Summary of "Concerning some additional aids in studying sedimentary formations" by M.S. Shuetsov. J. Sediment. Petrol. 25, 229–234.
Torres, M.E., Trehu, A.M., Cespedes, N., Kastner, M., Wortmann, U.G., Kim, J.H., Long, P., Malinverno, A., Pohlman, J.W., Riedel, M., Collett, T., 2008. Methane hydrate formation in turbidite sediments of northern Cascadia, IODP Expedition 311. Earth Planet. Sci. Lett. 271, 170–180.
Trehu, A.M., Long, P.E., Torres, M.E., Bohrmann, G., Rack, F.R., Collett, T.S., Goldberg, D.S., Milkov, A.V., Riedel, M., Schultheiss, P., Bangs, N.L., Barr, S.R., Borowski, W.S., Claypool, G.E., Delwiche, M.E., Dickens, G.R., Gracia, E., Guerin, G., Holland, M., Johnson, J.E., Lee, Y.J., Liu, C.S., Su, X., Teichert, B., Tomaru, H., Vanneste, M., Watanabe, M., Weinberger, J.L., 2004. Three-dimensional distribution of gas hydrate beneath southern Hydrate Ridge; constraints from ODP Leg 204. Earth Planet. Sci. Lett. 222, 845–862.
Uchida, T., Waseda, A., Namikawa, T., 2009. Methane accumulation and high concentration of gas hydrate in marine and terrestrial sandy sediments. AAPG Mem. 89, 45.
Ussler, W., Paull, C.K., 2001. Ion exclusion associated with marine gas hydrate deposits. In: Natural Gas Hydrates: Occurrence, Distribution, and Detection, pp. 41–51.
Wentworth, C.K., 1922. A scale of grade and class terms for clastic sediments. J. Geol. 30, 377–392.
White, R.J., Spinelli, G.A., Mozley, P.S., Dunbar, N.W., 2011. Importance of volcanic glass alteration to sediment stabilization: offshore Japan. Sedimentology 58, 1138–1154.
Winters, W., Walker, M., Hunter, R., Collett, T., Boswell, R., Rose, K., Waite, W., Torres, M., Patil, S., Dandekar, A., 2011. Physical properties of sediment from the Mount Elbert gas hydrate stratigraphic test well, Alaska North Slope. Mar. Petrol. Geol. 28, 361–380.